



HAL
open science

Volcanic tremors and magma wagging: gas flux interactions and forcing mechanism

David Bercovici, A. Mark Jellinek, Chloé Michaut, Diana Roman, Robert Morse

► **To cite this version:**

David Bercovici, A. Mark Jellinek, Chloé Michaut, Diana Roman, Robert Morse. Volcanic tremors and magma wagging: gas flux interactions and forcing mechanism. *Geophysical Journal International*, 2013, 195 (2), pp.1001-1022. 10.1093/gji/ggt277 . insu-02538766

HAL Id: insu-02538766

<https://insu.hal.science/insu-02538766>

Submitted on 9 Apr 2020

HAL is a multi-disciplinary open access archive for the deposit and dissemination of scientific research documents, whether they are published or not. The documents may come from teaching and research institutions in France or abroad, or from public or private research centers.

L'archive ouverte pluridisciplinaire **HAL**, est destinée au dépôt et à la diffusion de documents scientifiques de niveau recherche, publiés ou non, émanant des établissements d'enseignement et de recherche français ou étrangers, des laboratoires publics ou privés.

Volcanic tremors and magma wagging: gas flux interactions and forcing mechanism

David Bercovici,¹ A. Mark Jellinek,² Chloé Michaut,³ Diana C. Roman⁴
and Robert Morse^{1,*}

¹*Department of Geology & Geophysics, Yale University, New Haven, CT, USA. E-mail: david.bercovici@yale.edu*

²*Department of Earth, Ocean & Atmospheric Sciences, University of British Columbia, Vancouver BC, Canada*

³*Université Paris-Diderot, Sorbonne Paris Cité, IPG-Paris, F-75013, Paris, France*

⁴*Department of Terrestrial Magnetism, Carnegie Institution of Washington, Washington DC, USA*

Accepted 2013 July 10. Received 2013 July 9; in original form 2013 April 2

SUMMARY

Volcanic tremor is an important precursor to explosive eruptions and is ubiquitous across most silicic volcanic systems. Oscillations can persist for days and occur in a remarkably narrow frequency band (i.e. 0.5–7 Hz). The recently proposed magma-wagging model of Jellinek & Bercovici provides a basic explanation for the emergence and frequency evolution of tremor that is consistent with observations of many active silicic and andesitic volcanic systems. This model builds on work suggesting that the magma column rising in the volcanic conduit is surrounded by a permeable vesicular annulus of sheared bubbles. The magma-wagging model stipulates that the magma column rattles within the spring like foam of the annulus, and predicts oscillations at the range of observed tremor frequencies for a wide variety of volcanic environments. However, the viscous resistance of the magma column attenuates the oscillations and thus a forcing mechanism is required. Here we provide further development of the magma-wagging model and demonstrate that it implicitly has the requisite forcing to excite wagging behaviour. In particular, the extended model allows for gas flux through the annulus, which interacts with the wagging displacements and induces a Bernoulli effect that amplifies the oscillations. This effect leads to an instability involving growing oscillations at the lower end of the tremor frequency spectrum, and that drives the system against viscous damping of the wagging magma column. The fully non-linear model displays tremor oscillations associated with pulses in gas flux, analogous to observations of audible ‘chugging’. These oscillations also occur in clusters or envelopes that are consistent with observations of sporadic tremor envelopes. The wagging model further accurately predicts that seismic signals on opposite sides of a volcano are out of phase by approximately half a wagging or tremor period. Finally, peaks in gas flux occur at the end of the growing instability several tens of seconds after the largest tremors, which is consistent with observations of a 30- to 50-s lag between major tremor activity and maximum gas release. The extended magma-wagging model, thus, predicts tremor frequency and its evolution before and during an eruption, as well as a driving mechanism to keep the tremor excited for long periods.

Key words: Physics of magma and magma bodies; Explosive volcanism; Magma migration and fragmentation; Eruption mechanisms and flow emplacement; Volcano monitoring; Volcanic hazards and risks.

1 INTRODUCTION

The appearance of low-frequency tremor prior to explosive eruptions of silicic volcanoes is an important precursor for volcanological hazards. Volcanic tremor typically emerges well before an

eruption with frequencies in the range of 0.5–2 Hz, while during eruptions its frequency spectrum broadens to 5–7 Hz (Neuberg 2000; Konstantinou & Schindwein 2003; McNutt 2005; McNutt & Nishimura 2008; Jellinek & Bercovici 2011; Chouet & Matoza 2013).

As critical as volcanic tremor is to hazard mitigation, its cause remains enigmatic. A successful model for volcanic tremor must explain its excitation, longevity and the evolution of its frequency

* Now at: 23 Macdonnell Road, Apartment 202, Midlevels, Hong Kong SAR.

spectrum up to and including an eruption. Previous models have suggested that tremor can be caused by mechanical coupling of ascending magma to the conduit walls (Denlinger & Hoblitt 1999; Goto 1999); unsteady stirring in a gas-rich magma (Chouet 1996; Garcés *et al.* 1998; Hellweg 2000); and the interaction of ascending magma with volcanic conduit constrictions (Julian 1994) and wall cracks (Chouet 1996; Kumagai & Chouet 1999; Rust *et al.* 2008). The evolution of the frequency spectrum might be associated with changes in gas content, bubble size distribution, bubble nucleation depth and the conduit height and diameter (Chouet *et al.* 1997; Garcés *et al.* 1998; Sherburn *et al.* 1999; Neuberg 2000; Hagerty *et al.* 2000). Moreover, the geometry of conduit wall cracks (Hurst & Sherburn 1993; Neuberg 2000), and the depth of the brittle failure zone in the magma column (Goto 1999; Neuberg *et al.* 2006; Tuffen *et al.* 2008), may change the surface signal of oscillations. However, a limitation for these models is that the structure and constitution of the magma-conduit system is unlikely to be the same across volcanic environments or to be preserved during an eruption. In addition to variations in volcano size, differences in conduit erosion (Bryan & Sherburn 2003; McNutt & Nishimura 2008) and magma degassing (Sparks 2003) would, according to standard models, lead to large variations in the tremor frequency, which are not observed.

Recently we proposed a model for tremors based on the idea of oscillations of the entire magma column, termed the ‘magma-wagging’ model (Jellinek & Bercovici 2011). The model builds on observations and modelling that suggest that, in silicic systems, magma rises as a relatively stiff column surrounded by a gas-rich annulus (Okumura *et al.* 2006, 2008; Gonnermann & Manga 2007). In particular, shearing near the conduit causes bubbles entrained in the rising magma to stretch, coalesce and become inter-connected, thereby forming a vesicular, permeable and nearly shear-stress-free jacket surrounding the magma column (Eichelberger *et al.* 1986; Sparks 2003; Bluth & Rose 2004; Gonnermann & Manga 2007; Okumura *et al.* 2006, 2008). Analyses of pumice from effusive and explosive eruptions (Klug & Cashman 1996; Wright *et al.* 2009) demonstrate the development of elongated bubbles within the annulus that form a permeable tube-like matrix with porosity ϕ_o of 30–90 per cent. Thus gas can ascend relative to the magma column near the conduit wall (Eichelberger *et al.* 1986; Sparks 2003), as evident in gas rings rising at the edges of volcanic vents (Stasiuk *et al.* 1996; Bluth & Rose 2004; Sahetapy-Engel & Harris 2009). The depth H_0 over which the plug and annulus geometry is appropriate depends on the amount and solubility of volcanic gas (primarily H_2O), but is typically of order 1 km (Collier *et al.* 2006; Gonnermann & Manga 2007).

The magma-wagging model stipulates that volcanic tremor is a consequence of the magma column rattling or wagging inside the bubble-rich annulus. Specifically, lateral displacements of the column from its central resting position compress or dilate the annulus, which acts as a semi-permeable springy foam that restores the magma column to its resting state. The column’s inertia causes an over-shoot of this resting position, leading to a ‘wagging’ oscillation, whose impulse is imparted to the conduit walls to cause tremor. Jellinek & Bercovici (2011) demonstrated that this model predicted tremor oscillations in the range of observed frequencies; the model also explains the rise in frequency, sometimes indicated by gliding spectral lines (Neuberg 2000; Hotovec *et al.* 2013), and spectrum broadening in the eruptive phase, in terms of a narrowing and eventual fragmentation of the annulus during magma ascent. However, Jellinek & Bercovici (2011) also inferred that the viscous resistance of the magma column to bending would attenuate the oscillations over minutes and thus an unspecified driving mechanism was nec-

essary to excite the wagging oscillations. In this paper we demonstrate that, in fact, the same magma-wagging model implicitly has the requisite driving mechanism to excite the oscillations, and can explain other longer period behaviour, such as bursts of tremor envelopes (Johnson & Lees 2000; McNutt & Nishimura 2008; Lees *et al.* 2008; Zobin 2011). In particular, Jellinek & Bercovici (2011) focussed on an impermeable foam annulus model to predict the natural tremor frequency. However, the foam model does not permit gas flux through the annulus and thus cannot account for forcing or instabilities. A more complete permeable annulus model allows for a driving mechanism arising from the interaction of the gas flux and wagging. This interaction leads to a Bernoulli effect—wherein an increase (or decrease) in gas velocity induces a decrease (increase) in pressure—that amplifies the oscillation at moderate frequencies. More specifically, while the gas spring force in the annulus acts to restore the displaced magma column to its resting position, the pinching (or dilation) of the annulus causes an increase (or decrease) in the gas velocity that induces a pressure drop (or rise) that drives the displacement further. The competition between the gas spring force and the Bernoulli effect are critical components of the full magma-wagging mechanism. Therefore, we revisit and expand the development of the magma-wagging model, examine the predicted small- and large-amplitude oscillations and show that this basic model accounts for both natural tremors and a forcing mechanism self-consistently.

2 THE CYLINDRICAL FOAM ANNULUS MODEL REVISITED

To identify the key physics of the wagging oscillation, Jellinek & Bercovici (2011) analysed the idealized case of an impermeable foam annulus composed of unconnected compressible bubbles. This model predicts a free-oscillation frequency, but does not account for gas flux through the annulus, which potentially forces the oscillations. Nevertheless, here we summarize the foam annulus formulation to illustrate the basic concepts of the model before developing the more complete model.

We assume bubbles in the magma, and in particular foam in the annulus, move with the rising magma (which is reasonable for silicic magmas; Gonnermann & Manga 2007), and thus we affix the reference frame to the magma column. We assume the inner column of magma of radius R_m is cylindrically axisymmetric and initially at rest and centered inside the cylindrical conduit of radius R_c (Fig. 1). The resting width of the gap between the conduit wall and the inner column is $L = R_c - R_m$ (see also discussion of the non-linear Cartesian model in Section 4). We assume that lateral displacement of the column is only in the x - z plane; thus, when a vertical segment of the magma column at height z is displaced to the right by an amount $u(z)$, the maximum annular gap width is $L + u$ on the left, and the minimum gap width is $L - u$ on the right (see Fig. 1).

The net pressure force of the foam annulus exerted on a vertical segment of the magma column determines the oscillation restoring force. Since the foam acts like a compressible ideal gas, the pressure variations depend on how the volume of a parcel of foam is squeezed by the displacement of the magma column to the right (or left), for which we must determine the location of the magma column’s cylindrical surface. In a polar coordinate system centred on the axis of the conduit cylinder, the magma column’s cylindrical surface is given by

$$(r_m \cos \theta - u)^2 + (r_m \sin \theta)^2 = R_m^2, \quad (1)$$

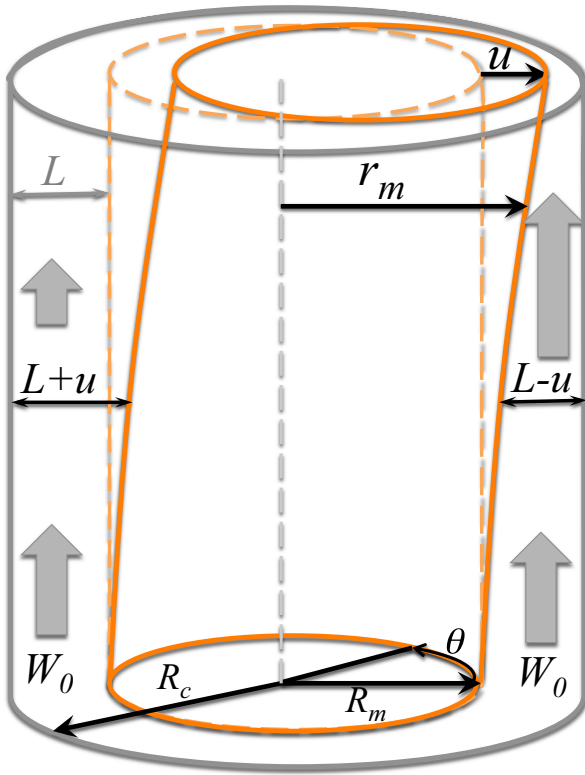


Figure 1. Sketch of the cylindrical annulus for the magma-wagging volcanic tremor model. The column is assumed to have a free surface at the top and is coupled viscously to the magma system below. The simpler impermeable foam annulus model (Section 2) has zero gas flux through the annulus, thus the input gas speed $W_0 = 0$ and the indicated vertical flow is neglected. The permeable annulus model (Section 3) accounts for gas flux wherein $W_0 \neq 0$ and the pinching or dilation of the annulus by bending of the magma column causes either faster or slower flow, respectively, as indicated. Variables displayed in the diagram are discussed in the accompanying text.

where r_m is the radial distance from the axis of the conduit to the magma column's vertical surface, and θ is the angle relative to the line of displacement (see Fig. 1). Assuming small displacements such that $u \ll R_m$, leads to

$$r_m(\theta, z) = R_m + u(z) \cos \theta. \quad (2)$$

The volume of a segment of foam in the annulus from θ to $\theta + d\theta$ and of vertical height dz is

$$V = dz d\theta \int_{r_m}^{R_c} r dr = \frac{1}{2} dz d\theta (R_c^2 - R_m^2 - 2u R_m \cos \theta), \quad (3)$$

while the undisturbed volume of this segment is $V_0 = \frac{1}{2} dz d\theta (R_c^2 - R_m^2)$; hence the volume of the segment can be written as

$$V = V_0 \left(1 - \frac{u}{U} \cos \theta \right), \quad \text{where } U = \frac{R_c^2 - R_m^2}{2R_m}, \quad (4)$$

and we note that $U \approx L$ in the limit of $L \ll R_m$. The gas volume V_g is only a portion of the segment's volume, but it can be inferred by assuming that the magma volume is conserved since magma is largely incompressible; this implies that $V - V_g = V_0 - V_{g0}$, where V_{g0} is the unperturbed gas volume, which leads to

$$V_g = V_0 \left(\phi_0 - \frac{u}{U} \cos \theta \right), \quad (5)$$

where $\phi_0 = V_{g0}/V_0$ is the unperturbed gas volume fraction. The gas pressure is then found using the ideal gas law

$$P = \frac{(M_0/m_g)\mathcal{R}T}{V_g} \approx \rho_0 C^2 \left(1 + \frac{u}{\phi_0 U} \cos \theta \right), \quad (6)$$

where we again assume infinitesimal displacements smaller than the gap width such that $u \ll U$; here M_0 is the mass of gas in the segment, which is conserved, $\rho_0 = M_0/(\phi_0 V_0)$ is the undisturbed gas density, \mathcal{R} is the gas constant, T is temperature, m_g is the molar mass of the gas and $C = \sqrt{\mathcal{R}T/m_g}$ is the isothermal gas sound speed (temperature is assumed to be constant since it is buffered by the relatively high heat capacity of the magma; e.g. see Bercovici & Michaut 2010). The traction (force/area) of the gas pressure pushing on the magma column in the direction of displacement is

$$-P \hat{x} \cdot \hat{n} \approx -P \left(\cos \theta - \frac{u}{R_m} \sin^2 \theta \right), \quad (7)$$

where \hat{x} and \hat{n} are the unit vectors in the direction of displacement and normal to the magma column's surface, respectively. Integrating this traction completely around the annulus (i.e. for $0 \leq \theta \leq 2\pi$) gives the net pressure force on a vertical segment of the magma column of thickness dz :

$$F_p = -dz \int_0^{2\pi} P(\theta) \hat{x} \cdot \hat{n} r_m(\theta) d\theta = -dz \rho_0 C^2 \frac{\pi R_m}{\phi_0 U} u. \quad (8)$$

The resistance force due to viscous bending of the column is given by the difference in shear tractions between the top and bottom of a column segment of height dz , that is,

$$F_b = [\tau_{xz}]_z^{z+dz} \pi R_m^2, \quad (9)$$

where τ_{xz} is the shear stress resisting the magma column bending to the left or right. We neglect elastic behaviour of the column because the Maxwell relaxation time for rhyolitic magmas with viscosities in the range of 10^5 – 10^9 Pa s and shear moduli in the corresponding range of 10^{10} – 10^{11} Pa (Bagdassarov *et al.* 1994) will be less than 10^{-1} – 10^{-2} s, which is shorter than the timescale of oscillations considered here; elastic effects can become significant at the highest tremor frequencies but the magma will still be predominantly viscous. At any given point in the column we can approximate (for small displacement) the stress as

$$\tau_{xz} = \mu_m \frac{\partial^2 u}{\partial z \partial t}, \quad (10)$$

where μ_m is the magma's dynamic viscosity.

Considering both gas pressure and viscous bending forces, Newton's second law for the segment of the magma column requires that

$$\rho_m \pi R_m^2 dz \frac{\partial^2 u}{\partial t^2} = -dz \rho_0 C^2 \frac{\pi R_m}{\phi_0 U} u + [\tau_{xz}]_z^{z+dz} \pi R_m^2, \quad (11)$$

which, in the limit of small dz , and using (10), becomes

$$\frac{\partial^2 u}{\partial t^2} = -\omega_0^2 u + \nu_m \frac{\partial^3 u}{\partial z^2 \partial t}, \quad (12)$$

where

$$\omega_0^2 = \frac{\rho_0 C^2}{\phi_0 \rho_m R_m U} = \frac{2\rho_0 C^2}{\phi_0 \rho_m (R_c^2 - R_m^2)} \quad \text{and} \quad \nu_m = \mu_m / \rho_m \quad (13)$$

are the natural oscillation frequency and kinematic viscosity of magma, respectively.

The predicted angular frequency ω_0 depends on various properties, the most poorly constrained of which is related to conduit

geometry, that is, on R_c and R_m , all other factors in the relation for ω_0 in (13) being well characterized by observations or experiments. However, since $\omega_0 \sim (R_c^2 - R_m^2)^{-1/2}$, the dependence on geometry is weak. In particular, if $10 \leq R_c \leq 100$ m and $0.5 \leq R_m/R_c < 1$ (and using $C = 700$ m s⁻¹, $\rho_m/\rho_0 = 100$ and $\rho_m = 2500$ kg m⁻³ for eruptions in which the gas is primarily water at about 1000 K, but neglecting the effects of gravity, which are considered later in Section 4), then the frequency of oscillations ranges from about 0.1 Hz to 5 Hz well within the range of known volcanic tremors (Jellinek & Bercovici 2011).

However, in general these oscillations are damped by viscous resistance to bending in the magma column, and their frequency and growth (or decay) rate depend on magma viscosity also. Assuming $u \sim e^{ikz + st}$, where k is wavenumber and s the growth rate, we arrive at a dispersion relation:

$$s = -v_m k^2/2 \pm \sqrt{(v_m k^2/2)^2 - \omega_0^2}. \quad (14)$$

Oscillations occur if $k < \sqrt{2\omega_0/v_m}$. Thus, as discussed in Jellinek & Bercovici (2011), with typical silicic magma properties, the oscillation wavelength $2\pi/k$ must exceed approximately 100 m for the oscillation to occur. However, the fundamental wagging mode (i.e. in which the entire magma column waves with a fixed base and a freely moving top, as illustrated in Fig. 1) corresponds to a wavelength of approximately $4H_0$ where H_0 is the magma column height, which is typically of order 1000 m; therefore, the oscillation should occur.

The oscillation is damped at a rate $v_m k^2/2$, or

$$\frac{v_m}{2} \left(\frac{\pi}{2H_0} \right)^2 \approx 5 \times 10^{-3} \text{ s}^{-1} \quad (15)$$

for the fundamental mode with $H_0 = 1$ km. Since tremors are sustained for hours or days, the oscillations would necessarily need to be excited by some forcing mechanism to overcome this damping. The foam model does not predict such forcing. However, as shown below, gas flux through a permeable annulus induces a natural instability that counters viscous damping and helps excite the wagging oscillation.

3 PERMEABLE CYLINDRICAL ANNULUS MODEL

Gas flow through the annulus provides a driving mechanism for the oscillations through a Bernoulli effect, which applies to both compressible and incompressible gases. In particular, while squeezing of the annulus and increasing gas pressure imposes a restoring force for the column oscillations, the same constriction causes gas velocity to increase by a nozzle effect. This increase in velocity on the pinched side of the annulus causes a pressure drop which draws the column displacement further in the same direction. In contrast, dilation of the annulus acts to rarify gas, thus lowering its pressure and opposing column displacement; yet, at the same time, the drop in gas velocity through the dilated annulus acts to increase pressure, which drives column displacement. This competition between gas compression/expansion and the Bernoulli effect during magma column displacement determines whether oscillations are excited or die away.

To allow for gas flux in the annulus, we revise the model so that the annulus is an interconnected pore space with finite permeability (again, see Fig. 1, but for the case with $W_0 \neq 0$), caused by the shearing of bubbles into tubes near the conduit wall (as implied by observations and microstructural analysis of tube pumice; e.g.

Wright *et al.* 2006). Gas flow in the annulus is driven both by gas injected from below, as well as by pressure variations arising from lateral displacement of the magma column and squeezing of the annulus. As with the foam model above, we assume for simplicity that variables (gas density, porosity, velocity, etc.) are independent of radial distance r from the centre of the conduit, that any variability in azimuthal angle θ is only caused by the horizontal displacement of the magma column, and that tubular bubbles in the annulus do not ascend relative to the magma column.

3.1 Equations of motion for the permeable annulus

3.1.1 Mass conservation

As with the foam annulus model, the motion of the magma column squeezes or dilates the pores, which in turn affects the gas density; however, in this case the gas can escape. We assume that the pores are drawn out primarily into vertical tubes, thus flow is predominantly in the vertical direction z . Conservation of mass for gas in a segment of the annulus from θ to $\theta + d\theta$, from z to $z + dz$ and $r = r_m(\theta)$ to $r = R_c$ requires

$$d\theta dz \frac{\partial}{\partial t} \int_{r_m}^{R_c} \rho \phi r dr = -d\theta dz \frac{\partial}{\partial z} \int_{r_m}^{R_c} \rho \phi w r dr, \quad (16)$$

where ρ is gas density, ϕ is porosity or gas volume fraction and w is the vertical velocity of gas relative to the magma. Assuming variables are functions of z and t but uniform across r , this relation leads to

$$\frac{\partial \rho \phi}{\partial t} + \frac{\partial \rho \phi w}{\partial z} = 0, \quad (17)$$

where

$$\phi = \phi \left(1 - \frac{u}{U} \cos \theta \right) \quad (18)$$

accounts for compression/dilation of the annulus segment by motion of the magma column (i.e. because r_m in the above integral limits is both z and t dependent).

We next use conservation of mass in the matrix surrounding the gas (i.e. the walls of the pores or tubes) to infer how porosity ϕ is affected by the motion of the central magma column. First, we state that the magma column rises at a constant velocity and that the coordinate system is fixed to this magma column. We also assume the magma matrix in the porous annulus remains fixed to the magma column. Finally, we assume that any wedge in a vertical slice of the porous annulus, that is, between θ and $\theta + d\theta$ and between z and $z + dz$, is uniformly squeezed (or dilated) by the horizontal deflection of the magma column. The mass of magma in this piece of porous annulus is conserved hence

$$\int_{r_m}^{R_c} \rho_m (1 - \phi) r dr = \int_{r_m}^{R_c} \rho_m (1 - \phi_0) r dr, \quad (19)$$

where ϕ_0 is the porosity of the undisturbed annulus. Since we assume ϕ remains uniform across r even when being squeezed (or equivalently that ϕ represents the average porosity across r), then

$$\phi = 1 - \frac{R_c^2 - R_m^2}{R_c^2 - r_m^2} (1 - \phi_0). \quad (20)$$

Again using $r_m = R_m + u \cos \theta$, then to first order in u

$$\phi = \phi_0 - (1 - \phi_0) \frac{u}{U} \cos \theta \quad \text{and} \quad \phi = \phi_0 - \frac{u}{U} \cos \theta, \quad (21)$$

which, once the gas velocity w is specified through momentum conservation, can be substituted into (17) to infer how density ρ changes with u and θ .

3.1.2 Momentum conservation

The conservation of momentum for vertical motion of gas in the pores or tubes in a segment of the annulus can be derived similarly to the above development for the mass of gas, and leads to

$$\frac{\partial}{\partial t} \int_{r_m}^{R_c} \rho \phi w r dr = -\frac{\partial}{\partial z} \int_{r_m}^{R_c} \phi (\rho w^2 + P) r dr - \phi P r_m \frac{\partial r_m}{\partial z} - \int_{r_m}^{R_c} \left(\phi \rho g - P \frac{\partial \phi}{\partial z} + c w \right) r dr. \quad (22)$$

The term on the left of (22) is the rate of change of gas momentum in the annulus at a height z ; the first term on the right accounts for the change in momentum flux and the vertical pressure gradient at z ; the second term on the right (proportional to $\partial r_m / \partial z$) is due to pressure acting vertically on the sloping surface of the magma column; and the last term on the right combines the effects of gravity, pressure acting on gradients in porosity and the inter-phase drag (where c is the coefficient of drag by the pore walls on the gas; see Bercovici & Michaut 2010). The drag force is only proportional to w because the coordinate system is fixed to the uniform-velocity magma reference frame. The shear traction from the conduit wall is neglected since it is already assumed to be effectively eliminated by the alignment and inter-connection of high-gas-fraction pores in the annulus.

With (17), the gas momentum relation (22) leads to the standard two-phase relation (see Bercovici & Michaut 2010):

$$\rho \phi \left(\frac{\partial w}{\partial t} + w \frac{\partial w}{\partial z} \right) = -\phi C^2 \frac{\partial \rho}{\partial z} - c w - \rho \phi g. \quad (23)$$

Because the coordinate system is fixed to the magma column and matrix, magma velocity does not appear; however, there are still forces exerted on the magma pore walls by pressure, drag and gravity. Since the matrix vertical velocity is assumed constant and uniform, the force balance on the matrix is

$$0 = -(1 - \phi) C^2 \frac{\partial \rho}{\partial z} + c w - \rho_m (1 - \phi) g, \quad (24)$$

where ρ_m is magma density (same as in the magma column), the gas and matrix pressures are assumed to be equal, and the drag of gas on magma in the pores/tubes is equal and opposite to the drag of magma on gas. Eqs (23) and (24) can be added to obtain

$$\rho \phi \left(\frac{\partial w}{\partial t} + w \frac{\partial w}{\partial z} \right) = -C^2 \frac{\partial \rho}{\partial z} - \bar{\rho} g, \quad (25)$$

where $\bar{\rho} = (1 - \phi) \rho_m + \phi \rho$. Alternatively one can take a weighted difference between (23) and (24) to eliminate the pressure gradient and obtain

$$\rho \phi (1 - \phi) \left(\frac{\partial w}{\partial t} + w \frac{\partial w}{\partial z} \right) = -c w + \phi (1 - \phi) (\rho_m - \rho) g. \quad (26)$$

Eq. (25) shows how gas is driven by vertical pressure gradients but against the weight of the entire mixture (i.e. not just the weight of the gas, but also the weight of matrix, which is dragging down on the gas). Eq. (26) shows how gas is equivalently driven by buoyancy (gas weight relative to matrix weight) but is retarded by drag. Both equations are equivalent, however, one expresses pressure gradients explicitly but the drag is in terms of matrix weight; while the other expresses drag explicitly but pressure gradients are in terms of gas

buoyancy. Eqs (17), (21) and (25) are sufficient to solve for gas density ρ and velocity w as functions of displacement u .

3.2 Equation of motion for the magma column

As with the foam annulus model, Newton's second law on a vertical segment of thickness dz of the magma column is

$$\rho_m \pi R_m^2 dz \frac{\partial^2 u}{\partial t^2} = -dz C^2 \int_0^{2\pi} \rho \hat{\mathbf{x}} \cdot \hat{\mathbf{n}} r_m d\theta + dz \mu_m \frac{\partial^3 u}{\partial z^2 \partial t} \pi R_m^2, \quad (27)$$

where we have again assumed the gas pressure is $C^2 \rho$. As with the foam model, we write $r_m = R_m + u \cos \theta$ and $\hat{\mathbf{x}} \cdot \hat{\mathbf{n}} = \cos \theta - (u/R_m) \sin^2 \theta$, thus to first order in u/R_m the momentum equation for the column becomes

$$\frac{\partial^2 u}{\partial t^2} = -\frac{C^2}{\rho_m \pi R_m^2} \int_0^{2\pi} \rho (R_m \cos \theta + u \cos(2\theta)) d\theta + \nu_m \frac{\partial^3 u}{\partial z^2 \partial t}, \quad (28)$$

where as before $\nu_m = \mu_m / \rho_m$ is the magma kinematic viscosity. If gas density and thus pressure were uniform around the annulus, the integral term on the right-hand side of (28) would be zero, hence there would be no restoring force on the column to sustain an oscillation.

3.3 Dimensionless governing equations

Eqs (17), (21), (25) and (28), comprise the governing equations for gas density ρ , volume fraction ϕ , velocity w and, finally, magma column displacement u . We non-dimensionalize these equations by selecting U for the length scale, U/C for a timescale and ρ_0 as a density scale (i.e. $\rho_0 U^3$ for mass scale). In this case we define (u, z) = $U(u', z')$, $t = U/C t'$, $w = C w'$ and $\rho = \rho_0 \rho'$ and the governing equations become (after dropping the primes)

$$\frac{\partial \rho \phi}{\partial t} + \frac{\partial \rho \phi w}{\partial z} = 0, \quad (29)$$

$$\rho \phi \left(\frac{\partial w}{\partial t} + w \frac{\partial w}{\partial z} \right) = -\frac{\partial \rho}{\partial z} - \gamma (\beta (1 - \phi) + \rho \phi), \quad (30)$$

$$\frac{\partial^2 u}{\partial t^2} = -\frac{2\lambda}{\beta\pi} \int_0^{2\pi} \rho (\cos \theta + 2\lambda u \cos(2\theta)) d\theta + \eta \frac{\partial^3 u}{\partial z^2 \partial t}, \quad (31)$$

where

$$\varphi = \phi_0 - u \cos \theta \quad \text{and} \quad \phi = \phi_0 - (1 - \phi_0) u \cos \theta \quad (32)$$

and we introduce the dimensionless numbers

$$\gamma = \frac{gU}{C^2}, \beta = \frac{\rho_m}{\rho_0}, \eta = \frac{\nu_m}{CU} \quad \text{and} \quad \lambda = \frac{U}{2R_m}. \quad (33)$$

Here, γ represents the ratio of hydrostatic and gas pressures, β is the ratio of magma and gas densities, η expresses the importance of viscous damping in the magma column relative to the gas spring force in the annulus and λ is a measure of the annulus thickness relative to the magma column width. In addition, we impose an injection gas velocity that is dimensionally W_0 , which non-dimensionally we refer to as the gas injection Mach number $\mathcal{M} = W_0/C$.

3.4 Linear oscillations and stability

Jellinek & Bercovici (2011, Supplementary Information) explored small amplitude oscillations to the permeable annulus problem to infer whether the fundamental tremor frequency was affected by gas flux in the annulus. They concluded that the fundamental frequency was unaffected even up to large gas injection velocities. Here we explore the full range of oscillations including one that is unstable and associated with the Bernoulli forcing mechanism. The original analysis of Jellinek & Bercovici (2011) allowed for the steady-state gas density to vary with height, but assumed that, over the domain length, the variation is small, as argued by Bercovici & Michaut (2010). However this only leads to constant background density and velocity with a small buoyancy effect on the perturbations, and little effect on the important oscillations and instabilities; thus the results differ little from assuming zero gravity in the first place. Moreover, whether the variations in background density are smaller than the perturbations themselves is arguable (Michaut *et al.* 2013) and depends on the domain height; thus it is simpler and self-consistent to assume $g = \gamma = 0$ for the linear stability analysis, which we do here.

To linearize the equations, we assume that the gas volume fraction or porosity is perturbed by the infinitesimal displacement of the column such that $u = \varepsilon u_1$, where $\varepsilon \ll 1$ (which we have in fact assumed intrinsically anyway by using small displacements) and thus

$$\phi = \phi_0 - (1 - \phi_0)\varepsilon u_1 \cos \theta \quad \text{and} \quad \varphi = \phi_0 - \varepsilon u_1 \cos \theta. \quad (34)$$

The gas flow and density with small perturbations to the steady state are expressed as

$$w = \mathcal{M} + \varepsilon w_1 \cos \theta \quad \text{and} \quad \rho = 1 + \varepsilon \rho_1 \cos \theta. \quad (35)$$

Substituting (34) and (35) into (29)–(31), we obtain to $O(\varepsilon)$

$$\left(\frac{\partial}{\partial t} + \mathcal{M} \frac{\partial}{\partial z} \right) (\phi_0 \rho_1 - u_1) + \phi_0 \frac{\partial w_1}{\partial z} = 0, \quad (36)$$

$$\phi_0 \left(\frac{\partial}{\partial t} + \mathcal{M} \frac{\partial}{\partial z} \right) w_1 + \frac{\partial \rho_1}{\partial z} = 0, \quad (37)$$

$$\frac{\partial^2 u_1}{\partial t^2} = -\phi_0 \alpha^2 \rho_1 + \eta \frac{\partial^3 u_1}{\partial z^2 \partial t}, \quad (38)$$

where $\alpha^2 = 2\lambda/(\phi_0\beta)$. Finally, stipulating that u_1 , w_1 and ρ_1 all go as e^{ikz+st} , we arrive at the characteristic equation

$$s^2 + \frac{\phi_0 \alpha^2 (s + ik\mathcal{M})^2}{k^2 + \phi_0 (s + ik\mathcal{M})^2} + \eta k^2 s = 0. \quad (39)$$

3.4.1 Some asymptotic dispersion relations

The characteristic eq. (39) is a fourth-order complex polynomial for the growth rate s , and thus has four possible roots that are, in general, algebraically cumbersome. However we can extract some important asymptotic relations from (39).

In the long-wavelength limit of $k \rightarrow 0$ we obtain from (39) $s = \pm i\alpha$, which dimensionally implies a free-oscillation frequency of

$$\omega_0 = \frac{\alpha C}{U} = \sqrt{\frac{2\lambda}{\phi_0\beta} \frac{C}{U}} = \sqrt{\frac{2\rho_0 C^2}{\phi_0 \rho_m (R_c^2 - R_m^2)}}, \quad (40)$$

which is the same as (13) for the foam-annulus model, with an angular frequency that corresponds to the 1 Hz tremor oscillation.

In the short-wavelength limit of $k \rightarrow \infty$ we can infer two possible solutions to (39). In one case, we assume that s grows with k and we write $s = ik\Omega$, that is, the perturbation is wave-like with dimensionless speed Ω ; this leads to

$$k^2 \Omega^2 + \frac{\phi_0 \alpha^2 (\Omega + \mathcal{M})^2}{1 - \phi_0 (\Omega + \mathcal{M})^2} - i\eta k^3 \Omega = 0. \quad (41)$$

For large η this leads to $\Omega = i\eta k$ or $s = -k^2 \eta$, and thus strong damping from viscous bending of the magma column (over short wavelengths), as expected. For $\eta \rightarrow 0$ and assuming that $\Omega \gg \mathcal{M}$ (i.e. the wave is comparable to a sound wave) we obtain

$$\Omega \approx \pm \sqrt{\frac{1}{\phi_0} + \frac{\alpha^2}{k^2}} \approx \pm \sqrt{\frac{1}{\phi_0}}. \quad (42)$$

Dimensionally this corresponds to a perturbation wave speed $C\Omega \approx C/\sqrt{\phi_0}$, which represents high frequency (small wavelength) disturbances propagating as sound waves in the annulus; however, these waves travel slightly faster than the normal gas sound speed, due to the higher effective compressibility imposed by the magma pore walls in the annulus (see Bercovici & Michaut 2010).

In the other case for large k , we assume s does not increase with k and this leads to

$$s \approx \frac{\phi_0 \alpha^2 \mathcal{M}^2}{\eta (1 - \phi_0 \mathcal{M}^2) k^2}, \quad (43)$$

which corresponds to a growing perturbation with a weak (or non-existent) oscillation (assuming $\mathcal{M} < 1$). This case corresponds to the one unstable branch of possible solutions that is associated with the Bernoulli driving effect and the resulting instability; indeed, the Bernoulli effect is manifest in the dependence of the growth rate on the square of the gas injection speed \mathcal{M}^2 , since the dynamic pressure from gas flow goes as ρw^2 , and the magnitude of w is dictated by \mathcal{M} . However, in general the maximum growth rate of the instability occurs at moderate wave-numbers and has a finite oscillation frequency (see Section 3.4.2).

3.4.2 General dispersion relation

The general dispersion relation results from solutions to the fourth-order complex polynomial from (39). Typical values for dimensionless parameters are $0.1 < \mathcal{M} < 0.5$, $0.01 < \lambda < 0.1$ (corresponding to a 10–100 m diameter magma column and a 1-m-wide annular gap), and $5 < \eta < 50$ (corresponding to $10^6 < \mu_m < 10^7$ Pa s). The solutions for all four roots to (39) are shown in Fig. 2 for some sample characteristic parameter values.

As discussed in Section 3.4.1, for long wavelengths (as $k \rightarrow 0$) the system has a high-frequency oscillation at a dimensionless angular frequency of $\sqrt{2\lambda/(\phi_0\beta)}$ which corresponds to the 1 Hz tremor [see (40) and black curves in Fig. 2] and is identical to that predicted by the closed foam annulus model. For smaller wavelengths (higher k) these oscillations propagate like sound waves as anticipated by (42).

3.4.3 Unstable, growing oscillations

The dispersion curves for the linear system display two sets of low-frequency oscillations (Fig. 2, blue curves). One of these low-frequency oscillations is unstable [i.e. has a positive growth rate, as also predicted in the high k limit in (43)], and has a peak growth rate at a finite wavelength, and thus a selected fastest growing mode. The positive growth rate curve is a strong function of the injection Mach

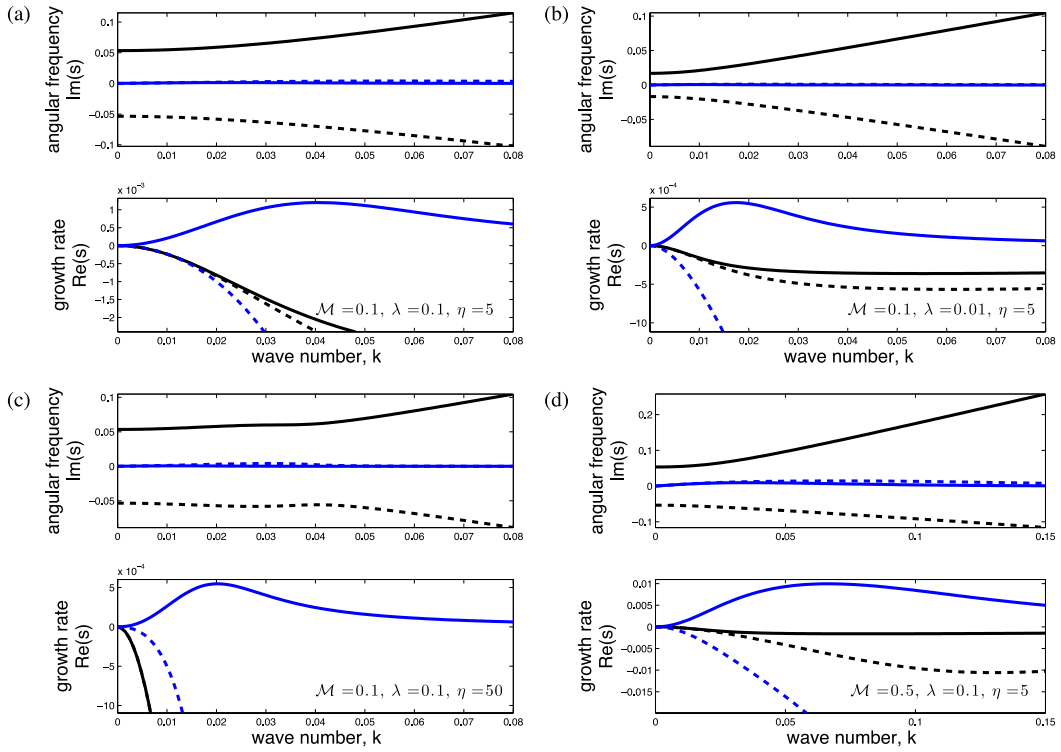


Figure 2. Non-dimensional dispersion curves for oscillation frequency and associated growth rate versus wavenumber for perturbations in the permeable annulus model (applicable to either cylindrical or Cartesian models). The dimensionalizing length scale is $U \approx L = R_c - R_m \approx 1\text{--}10$ m, and the dimensionalizing rate scale for both frequency and growth rate is $C/L \approx 70\text{--}700$ s $^{-1}$. Thus curves with large absolute dimensionless frequencies of around 0.05 (black curves) correlate to the high-frequency oscillation between a few to a few tens of Hz for low wavenumbers as predicted by (40), although at high wavenumbers they correspond to sound waves, as predicted by (42). Blue curves correspond to lower frequency oscillations that dimensionally are a few tenths to a few Hz, and one of which show a positive growth-rate instability, predicted by (43). Curves with positive frequencies represent upward propagating oscillations, and negative frequencies imply downward propagation; the solid and dashed curves indicate modes with equal and opposite frequencies. The maximum dimensionless growth rates are approximately $10^{-3}\text{--}10^{-2}$, which correspond to growth rates between $0.1\text{--}10$ s $^{-1}$. The wavelength of the fundamental mode $4H$ corresponds to a dimensionless wave number of $\pi L/(2H) \approx 10^{-3}\text{--}10^{-2}$, which are the smallest wavenumbers displayed. The dimensionless wavenumbers of the fastest growing modes occur around $k = 0.02\text{--}0.07$, which corresponds to dimensional wavelengths of approximately $90\text{--}3000$ m. Results are shown for various parameters as indicated, and for all cases $\phi_0 = 0.7$, $\beta = 100$ and $\gamma = 0$.

number \mathcal{M} , and moderately weak function of η and λ (Fig. 3). Indeed the instability does not occur unless $\mathcal{M} > 0$ and grows more rapidly for faster gas injection (Fig. 4), again as predicted by (43). An increase in magma column viscosity has little effect on the peak growth-rate of the instability, but shifts the wavenumber of the least stable mode to slightly smaller values (i.e. to longer wavelengths). Widening of the annular gap increases the growth-rate of the instability slightly and moves the least stable mode to higher wavenumbers (shorter wavelengths). The strong dependence of the instability on \mathcal{M} indicates that it is driven by a Bernoulli effect induced by flow of gas through annulus. This instability therefore provides a driving force that keeps the magma column oscillating despite viscous resistance of the magma itself.

3.4.4 Surface signature of linear oscillations

The solutions for u , ρ_1 and w_1 in the linear system can be used to infer a time-series for oscillations in displacement at the surface of the magma column $z = H$, where $H = H_0/U \approx H_0/L$ is the dimensionless column height. For a given wavenumber k the displacement at the top is given by

$$u(H, t) = \sum_{j=1}^4 \mathbf{u}_j e^{s_j t}, \quad (44)$$

where s_j represents the j -th root of (39). The initial conditions at $t = 0$ are that at $z = H$, perturbations u_1 , ρ_1 and w_1 are zero but that $\partial u_1 / \partial t = v_0$ (i.e. an initial perturbing velocity). Eqs (36) and (37) can then be used to express gas density and velocity perturbations as functions of u , and the four initial conditions then lead to

$$\sum_{j=1}^4 \left(1, s_j, \frac{\varpi_j}{\phi_0 \varpi_j^2 - k^2}, \frac{\varpi_j^2}{\phi_0 \varpi_j^2 - k^2} \right) \mathbf{u}_j = (0, v_0, 0, 0), \quad (45)$$

where $\varpi_j = i s_j - k \mathcal{M}$; this 4×4 linear system can be solved for the amplitudes \mathbf{u}_j from which the time-series of surface displacement (44) can be inferred. As a linear mock-up of possible oscillations, we superpose the displacements for two wavenumbers, namely for (a) the longest wavelength fundamental mode $k = \pi/(2H)$ which corresponds to the slowest decay of the high-frequency oscillations, and (b) the k for the fastest growing oscillation which will dominate the system after some time. This superposition captures the initial dominant high-frequency oscillation (comparable to the 1 Hz tremor) and then the subsequent growth of the most unstable long-period mode (Fig. 5). For moderate \mathcal{M} , the high-frequency oscillations will ring for some time (depending on η) before exponential growth of the low-frequency oscillations becomes significant; but as \mathcal{M} is increased, the instability happens faster before many of the high-frequency oscillations can occur (Fig. 5).

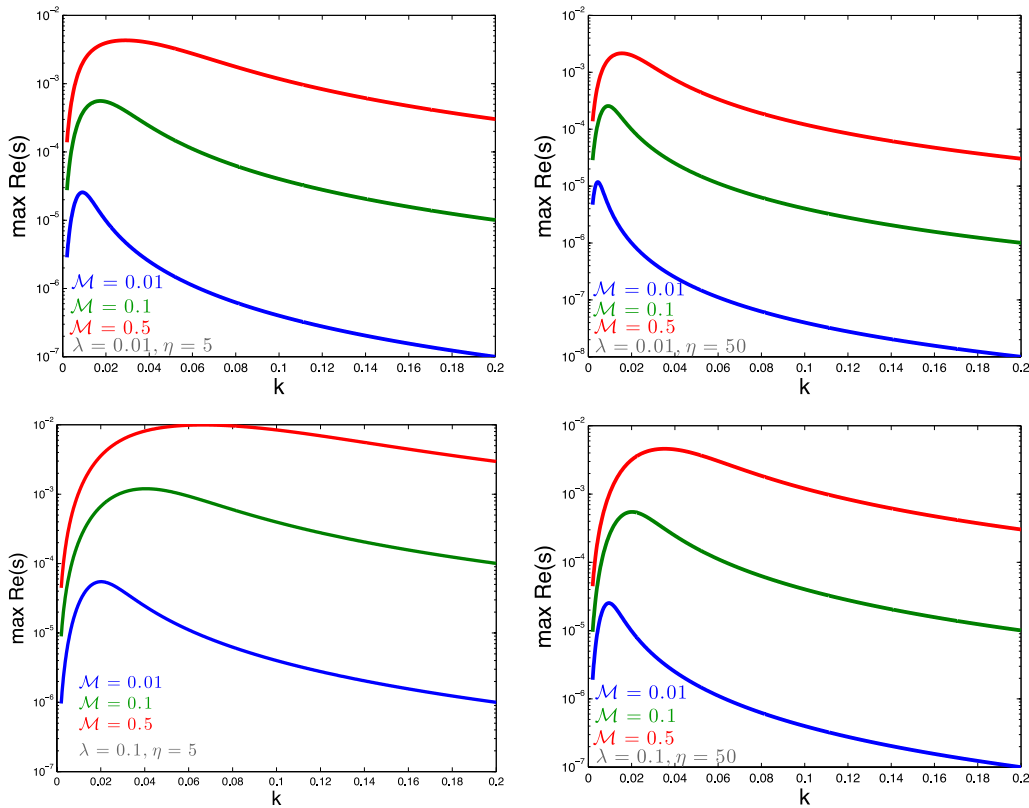


Figure 3. Dimensionless growth rate $\text{Re}(s)$ versus wavenumber for the unstable oscillation, for a range of \mathcal{M} and selected λ and η . See Fig. 2 for dimensionalizing scales.

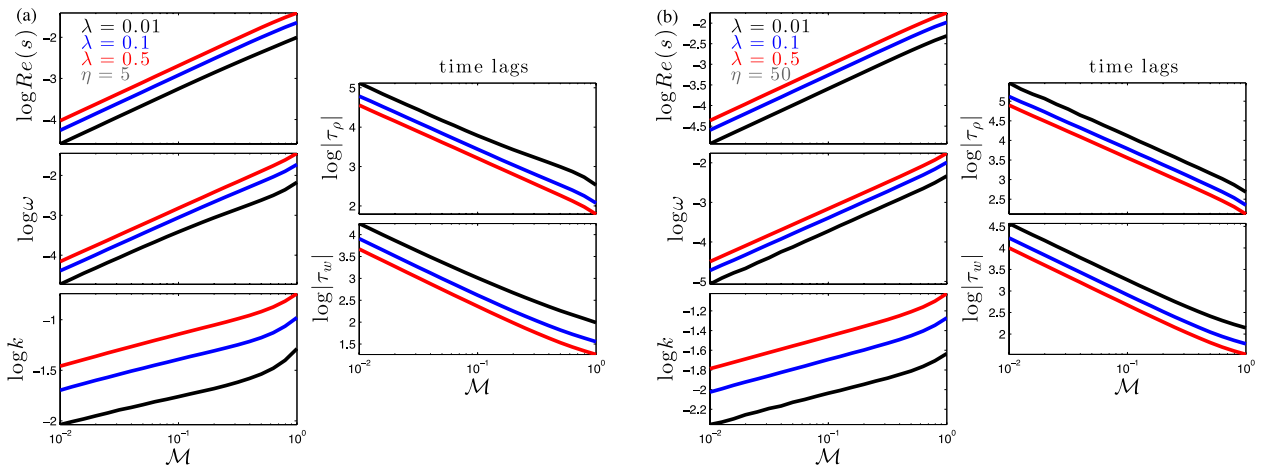


Figure 4. Growth rate, wavenumber and angular frequency for the least stable mode (i.e. the maximum $\text{Re}(s)$), as shown by the peaks in the curves in Fig. 3) versus \mathcal{M} and some select λ and η . Also shown are the time lags τ between oscillations in displacement and both gas density and vertical velocity; see Section 3.4.5.

3.4.5 Magma-column response to gas-flux

The linearized model can also be used to infer the response of the magma column to gas-flux during the fastest growing unstable oscillations. Considering only the least stable mode, the surface displacement of the magma column (44) can be expressed as

$$u_1(H, t) = \text{Re}(u_m e^{s_m t}) = \mathcal{U} \sin(\omega_m(t - t_0)) e^{\sigma_m t}, \quad (46)$$

where u_m and s_m are u_j and s_j for the least stable mode of the unstable oscillation (i.e. at which $\text{Re}(s)$ is a maximum) and $\sigma_m = \text{Re}(s_m)$ and $\omega_m = -\text{Im}(s_m)$. Moreover, t_0 is a sufficiently large time (such that the least-stable mode is dominant) at which the surface dis-

placement passes through zero [i.e. $u(H, t_0) = 0$]; this requires that $\mathcal{U} = -\text{Re}(u_m) / \sin(\omega_m t_0) = \text{Im}(u_m) / \cos(\omega_m t_0)$. Pulses in gas density or velocity are related to displacement generically as

$$\begin{aligned} \Theta(H) &= \text{Re}(\mathcal{G} u_m e^{s_m t}) \\ &= \mathcal{G} \mathcal{U} \sin(\omega_m(t - t_0 - \tau)) e^{\sigma_m t}, \text{ where } \mathcal{G} = G e^{i\omega_m \tau}, \end{aligned} \quad (47)$$

where Θ represents either perturbations in density ρ or velocity w at the surface, \mathcal{G} is the response operator, G is the response amplitude and τ is the time lag between the surface displacement and gas pulses. Eqs (36) and (37) with the normal mode analysis can be

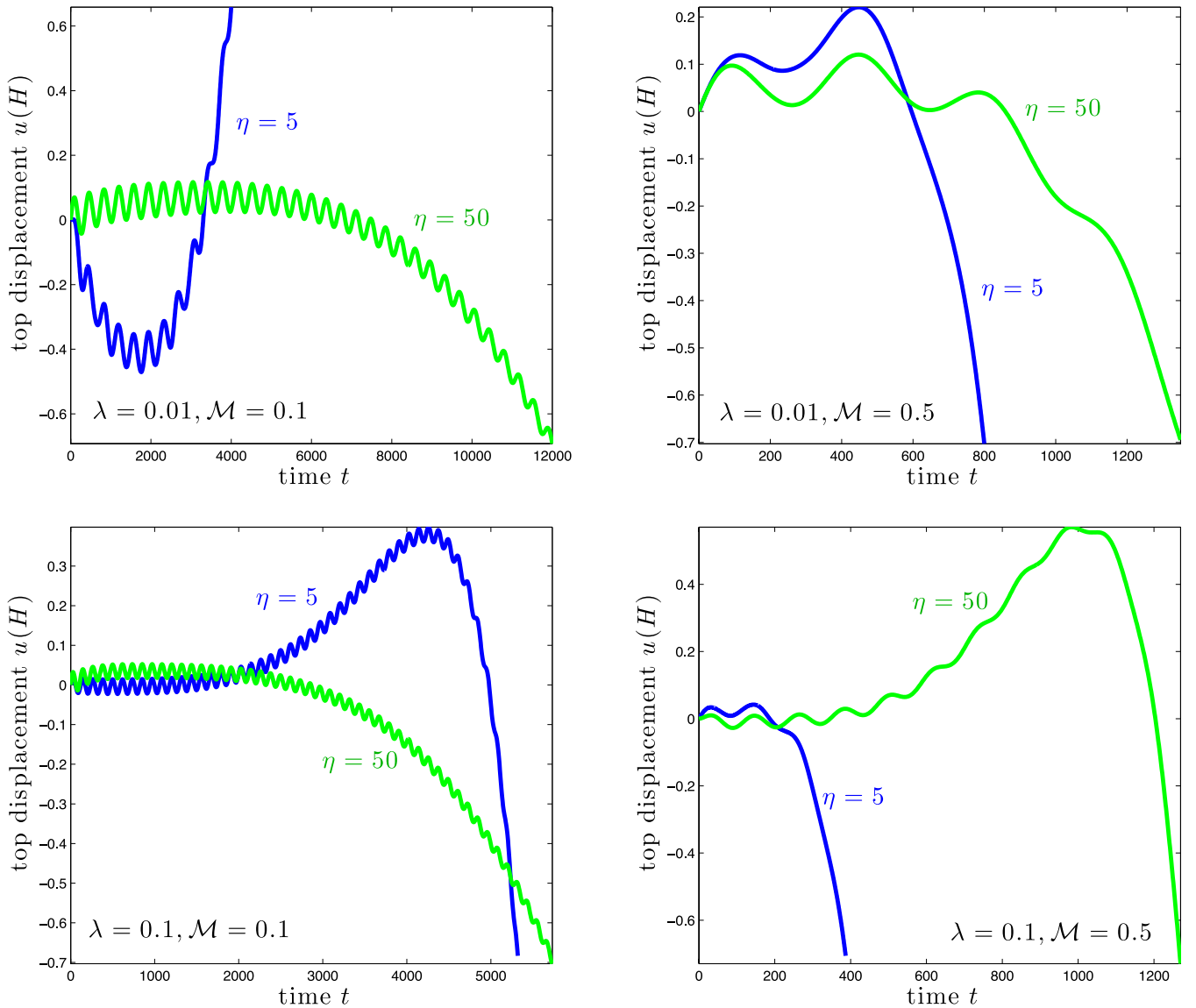


Figure 5. Oscillations in displacement u of the magma column at the column top $z = H$, as predicted by the linear stability analysis (see Section 3.4.4). The oscillations are the superposition of only two modes, the fundamental mode with wavenumber $k = \pi/(2H)$ and the least stable mode, as shown in Figs 3 and 4. Each mode is initiated with a velocity at $z = H$ of $v_0 = 10^{-3} \sin(kH)$, consistent with the non-linear numerical experiments. Figures shown are for various values of \mathcal{M} , λ and η as indicated. Cases with $\mathcal{M} = 0.1$ use a dimensionless domain height of $H = 1000$. However, because the density discontinuity or choking point in the non-linear solutions occurs at $H_c = 543$ for $\mathcal{M} = 0.5$ [see (62) and immediately subsequent discussion], the non-linear solutions in these cases use $H = 500$; and hence we use the same H for the corresponding linear cases shown here. All frames have the same values of $\phi_0 = 0.7$, $\beta = 100$ and $\gamma = 0$.

used to show that pulses in gas density and vertical velocity at the surface have response operators

$$\mathcal{G}_\rho = \frac{(s_m + ik_m \mathcal{M})^2}{k_m^2 + \phi_0 (s_m + ik_m \mathcal{M})^2}, \quad (48a)$$

$$\mathcal{G}_w = \frac{-ik_m (s_m + ik_m \mathcal{M})}{\phi_0 (k_m^2 + \phi_0 (s_m + ik_m \mathcal{M})^2)}, \quad (48b)$$

respectively, where k_m is the wavenumber of the least stable mode; using (47), each response is associated with time lags τ_ρ and τ_w for density and velocity pulses, respectively.

The time lags are perhaps most informative about the magma-column response (Fig. 4). In particular, the velocity time lag is generally negative, while that for density is positive; this means a gas velocity pulse arrives at the surface a time τ_w before the

associated peak in column displacement, while the density pulses arrives a time τ_ρ after the displacement peak. The dimensionless time lag is a modest function of magma viscosity, but a strong function of injection flux \mathcal{M} , being large for small \mathcal{M} and dropping rapidly for larger \mathcal{M} . Assuming a length scale $U \approx L = R_c - R_m \approx 1$ m, sound speed $C = 700$ m s $^{-1}$, then the dimensional time lag goes from nearly zero at large \mathcal{M} to about 3–7 min (depending on η) for gas density pulses, and 25–50 s for gas velocity pulses, at low \mathcal{M} .

Given the Bernoulli effect, the gas velocity pulses provide the main driving force for column displacement. As the velocity pulse propagates through one side of the annulus, it induces a low-pressure that pulls the column to the same side; but the column's viscosity causes a delayed response and thus the displacement lags behind the velocity pulse. With larger injection flux, represented by \mathcal{M} ,

the forcing is stronger, hence the response more immediate and the lag smaller. The gas density also responds to the Bernoulli effect by becoming low where the velocity pulse propagates (given the associated drop in pressure), and thus a positive pulse in gas density only comes in the wake of the column's displacement, that is, as gas reaccumulates behind the constricted annulus; hence the density pulse slowly lags the column's displacement.

These time lags, however, have more to do with the timing of bursts in tremor activity than in lags between tremor and gas pulses (which are discussed below in Section 5.3). In particular, the unstable growth in column displacement is relatively slow with low acceleration (i.e. long period and slow growth rates), and hence small induced ground motion, unrelated to the higher-frequency tremor. However the unstable column displacement eventually closes the annulus at various points, which cuts off the gas flux and the driving force for oscillations in that vertical plane (see non-linear model results, Section 4); in this case the leading gas velocity pulse is the last big puff of gas before closure, and the lagging density pulse is the subsequent build up of gas that likely leads to the instability and motion starting again in a different plane.

4 NON-LINEAR CARTESIAN MODEL AND FINITE AMPLITUDE ANALYSIS

To examine the growth of the unstable oscillation in the permeable annulus at finite amplitude we compose a modified set of equations for numerical analysis. In particular since the oscillation is assumed to stay in the x - z plane (in the plane of original 'wagging') we use a 2-D model, which allows us to relax the small displacement assumption required in the cylindrical model.

4.1 Governing equations

The development of the 2-D model follows the same logic as the cylindrical one, thus we develop the governing equations here only briefly. We consider conservation laws for material in the annulus, but treat the annulus now as two separate 2-D permeable vertical channels on either side of the magma column (Fig. 6). The magma column has width $2R_m$ (as in the cylindrical model) and at any given height z , the side channels have a gap width given by $L_i = L \pm u(z, t)$, where $L = R_c - R_m$ is the static gap width, u is again the displacement of the column, positive if to the right (in the positive x direction). The subscript $i = 1$ indicates the left channel and $i = 2$ is for the right channel; thus if $u > 0$ the left channel is wider at that height (i.e. with width $L + u$), and the right one equivalently narrower (see Fig. 6).

4.1.1 Mass conservation in the permeable side channels

Conservation of mass in a given channel segment between z and $z + dz$ and between the magma column's vertical surface at $x = R_c - L_i$ and the conduit wall at $x = R_c$ requires

$$dz \frac{\partial}{\partial t} \int_{R_c - L_i}^{R_c} \rho_i \phi_i dx = -dz \frac{\partial}{\partial z} \int_{R_c - L_i}^{R_c} \rho_i \phi_i w_i dx, \quad (49)$$

where ρ_i , ϕ_i and w_i are as previously defined but for the left ($i = 1$) and right ($i = 2$) channels. Assuming variables are uniform across x , this relation leads to

$$\frac{\partial \rho_i \phi_i}{\partial t} + \frac{\partial \rho_i \phi_i w_i}{\partial z} = 0, \quad (50)$$

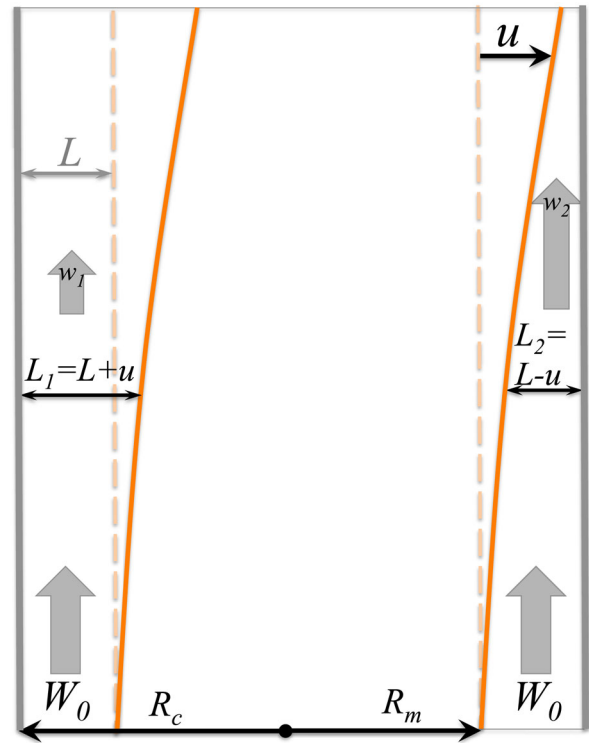


Figure 6. Sketch of 2-D non-linear model of volcanic tremor. See also Fig. 1.

where now

$$\phi_i = \phi_i \left(1 \pm \frac{u}{L} \right). \quad (51)$$

Mass conservation of the magma component of the annulus also requires

$$\int_{R_c - L_i}^{R_c} \rho_m (1 - \phi_i) dx = \int_{R_c - L}^{R_c} \rho_m (1 - \phi_0) dx, \quad (52)$$

where ϕ_0 is the undisturbed porosity and ρ_m is again magma density; this eventually yields

$$\phi_i = \frac{\phi_0 \pm u/L}{1 \pm u/L} \quad \text{and thus} \quad \phi_i = \phi_0 \pm u/L. \quad (53)$$

Although the expressions for ϕ_i and ϕ_i are similar to those for the linearized cylindrical model, they are not restricted to small displacements of the magma column.

4.1.2 Momentum conservation in the side channels

Momentum conservation for the permeable mixture in the side channels is developed identically to that for the annulus in the cylindrical model, and leads to

$$\rho_i \phi_i \left(\frac{\partial w_i}{\partial t} + w_i \frac{\partial w_i}{\partial z} \right) = -C^2 \frac{\partial \rho_i}{\partial z} - \bar{\rho}_i g, \quad (54)$$

where we have assumed, as with the cylindrical model, that there is no vertical variation in the matrix velocity.

4.1.3 Momentum conservation of the magma column

Newton's Second Law for the magma column in 2-D is similar again to the cylindrical model but leads to a slightly simpler version

$$\frac{\partial^2 u}{\partial t^2} = -\frac{C^2}{2\rho_m R_m}(\rho_2 - \rho_1) + v_m \frac{\partial^3 u}{\partial z^2 \partial t} \quad (55)$$

because the magma column in 2-D is a rectangle of width $2R_m$. The second term on the right-hand side of (55) represents the pressure difference between the right and left gaps at a given height z .

4.1.4 Dimensionless governing equations

We non-dimensionalize length by $L = R_c - R_m$ (which is similar to that in the cylindrical model since $U \approx L$ in the limit of small gap width; see Section 2), time by L/C , and density by the gas density at the point of injection ρ_0 . In this case, the dimensionless version of the governing equations, (50), (54) and (55), are

$$\frac{\partial \rho_i \phi_i}{\partial t} + \frac{\partial \rho_i \phi_i w_i}{\partial z} = 0, \quad (56)$$

$$\rho_i \phi_i \left(\frac{\partial w_i}{\partial t} + w_i \frac{\partial w_i}{\partial z} \right) = -\frac{\partial \rho_i}{\partial z} - \gamma(\rho_i \phi_i + \beta(1 - \phi_i)), \quad (57)$$

$$\frac{\partial^2 u}{\partial t^2} = -\frac{\lambda}{\beta}(\rho_2 - \rho_1) + \eta \frac{\partial^3 u}{\partial z^2 \partial t}, \quad (58)$$

where

$$\phi_i = \frac{\phi_0 \pm u}{1 \pm u} \quad \text{and} \quad \varphi_i = \phi_0 \pm u \quad (59)$$

and we are left with a similar set of dimensionless parameters

$$\gamma = \frac{gL}{C^2}, \beta = \frac{\rho_m}{\rho_0}, \eta = \frac{v_m}{CL} \quad \text{and} \quad \lambda = \frac{L}{2R_m}. \quad (60)$$

As in the cylindrical model, we impose an input velocity W_0 , which non-dimensionally is the gas injection Mach number $\mathcal{M} = W_0/C$. As noted above, one minor difference between the Cartesian and cylindrical models is that length is non-dimensionalized by L instead of U [see (33)]. However, given the definition of U from (4), $U = L(1 + \lambda)$, using the current definition of λ above; since we expect $\lambda \ll 1$, then $U \approx L$. Therefore, λ , γ and η are approximately the same as in the cylindrical model.

4.1.5 Note on Cartesian linear analysis

The linear wave and stability analysis of the Cartesian model can be done similarly to the cylindrical model by assuming a small displacement $u = \varepsilon u_1$ and expanding other dependent variables similarly to (34) and (35)—except instead of $\cos \theta$ dependence there are relations for the right and left channels. The final resulting characteristic relation for the growth rate s is identical to (39) and hence the linear analysis is identical to that presented in Section 3.4.

4.2 Non-linear steady-state analytic solutions

Non-linear solutions for the steady-state 'non-wagging' case provide both an important bench-mark for the full non-linear solutions, and also dictate the domain of non-linear calculations. In particular, these solutions are singular at a finite height z , which is the choking level for an expanding gas, that is, the point at which the gas velocity reaches the effective sound speed and the density develops a

discontinuity or a shock. The steady-state versions of (56) and (57) for $u = 0$ are the same in both annular channels, and they combine to yield

$$\frac{\partial \rho}{\partial z} = -\gamma \frac{\rho \phi_0 + \beta(1 - \phi_0)}{1 - \phi_0 \mathcal{M}^2 / \rho^2}, \quad (61)$$

where we have used the boundary condition that $\rho = 1$ and $w = \mathcal{M}$ at $z = 0$, and thus, because of (56) in steady state, that $w = \mathcal{M}/\rho$. According to (61), the density gradient becomes singular at $\rho = \mathcal{M}\sqrt{\phi_0}$, which is the choking point or shock (see Vergnolle & Jaupart 1986; Kozono & Koyaguchi 2009a,b; Bercovici & Michaut 2010). At the choking point, the gas speed is $w = \mathcal{M}/\rho = 1/\sqrt{\phi_0}$; this is dimensionally $C/\sqrt{\phi_0}$, which is slightly in excess of the gas sound speed, given the extra compressibility imposed by the matrix [see also (42)]. The general solution to (61) is given by the implicit solution

$$z(\rho) = \frac{\phi_0^2 \mathcal{M}^2}{\gamma \beta^2 (1 - \phi_0)^2} \left[\log \left(\frac{\rho \phi_0 + \beta(1 - \phi_0)}{\rho \phi_0 + \beta(1 - \phi_0)} \right) - \frac{\beta(1 - \phi_0)(1 - \rho)}{\phi_0 \rho} \right] + \log \left(\frac{\phi_0 + \beta(1 - \phi_0)}{\rho \phi_0 + \beta(1 - \phi_0)} \right)^{\frac{1}{\phi_0 \gamma}}. \quad (62)$$

The height of the choking point occurs at $H_c = z(\mathcal{M}\sqrt{\phi_0})$, and we define this singularity as the upper limit of our domain.

4.3 Numerical experiments

4.3.1 Solution method

The coupled non-linear equations for motion in the annular channels and magma column (56)–(58) are solved numerically using finite differences in which the gas velocities in the annular channels w_i are on a staggered grid relative to densities ρ_i and column displacement u . Advection terms are treated with upwind differencing (which is second-order accurate on the staggered grid), while divergence and diffusion are treated with centred difference (i.e. again second-order accurate). Time integration uses a semi-implicit Crank–Nicolson scheme and a Courant–Friedrichs–Lewy (CFL) time step condition based on the gas velocity w_i (Roache 1976). The magma column momentum eq. (58) is separated into two first-order differential equations in time by introducing the lateral magma column velocity v and the equation $\frac{\partial u}{\partial t} = v$.

The bottom boundary conditions are $u = v = 0$, $\rho_i = 1$ and $w_i = \mathcal{M}$ at $z = 0$. The top of the domain at $z = H$ is open and arbitrary since it must be located below the choking point such that $H < H_c$ (see Section 4.2). Strictly speaking only (58) requires a second boundary condition at $z = H$, since it is a forced diffusion equation for v ; and for this we choose $\frac{\partial v}{\partial z} = 0$ at $z = H$ assuming there are no stresses or forces driving the column for $z > H$. Because w_i is on the staggered grid, its last value is at $z = H + \Delta z/2$, where Δz is the grid spacing; solution of (57) at this point thus requires an estimate of the gas density ρ_i at the super-domain point $z = H + \Delta z$. Because the super-domain-point approaches the choking point and a density discontinuity, simple extrapolations of density to this level (either linear, quadratic or even cubic) are too imprecise and introduce errors and numerical instabilities. Hence the density is assumed to obey (61) at the super-domain point; that is, this equation is used to extrapolate density that is at least consistent with the known steady-state analytic solution.

At time $t = 0$ the gas velocity and density are initiated with the non-linear analytic solutions for $u = 0$, but the magma lateral

velocity is perturbed with the fundamental mode or quarter-wave $v = \varepsilon \sin(\pi z/(2H))$ (i.e. with a wavelength of $4H$) where $\varepsilon \ll 1$ (typically we set $\varepsilon = 10^{-3}$).

The numerical solutions are bench-marked against the linear stability in the limit $\gamma \rightarrow 0$, as well as the non-linear steady-state solution (62); solutions are found to be accurate for at least 50 gridpoints, although the final solutions never involve less than 100 points. Given the semi-implicit time integration, the maximum allowable time step obeys the CFL condition, but this is further reduced by a factor that is typically 10^{-2} – 10^{-4} to ensure convergence of solutions.

Table 1. Table of dimensionless parameters for the linear and non-linear models.

Parameter	Definition	Value (s)
γ	gL/C^2	2×10^{-5}
β	ρ_m/ρ_0	100
\mathcal{M}	W_0/C	0.1–0.5
λ	$L/(2R_m)$	0.01–0.1
η	$\nu_m/(LC)$	5–50
H	z_{\max}/L	500–1000

4.3.2 Results

We explore numerical solutions with the same approach for the linear cases, that is, to determine the forcing and growth of the ‘wagging’ instability for various parameter choices. In particular, we examine the sensitivity of solutions to different injection velocities or Mach numbers \mathcal{M} , each for different gap aspect ratios $\lambda = L/(2R_m)$ and magma dimensionless viscosities $\eta = \nu_m/(CL)$. Parameter values are displayed in Table 1.

The numerical solutions qualitatively match the linear stability results even for $\gamma \neq 0$. The magma column initially oscillates with small amplitude oscillation with a dimensionless frequency of approximately 10^{-2} , which dimensionally is near the 1 Hz oscillation (given that we use $L = 1$ – 10 m and $C = 700$ m s $^{-1}$). Depending on the parameter choice this oscillation damps either slowly or moderately fast (though rarely entirely) and gives way to an oscillation with a lower frequency of around 10^{-3} (i.e. a few tenths of a Hz) and a growth rate of comparable value (see Figs 7 and 8, each of which provide a URL link to movies that better display the time-dependent behaviour; other sample figures are shown in the Appendix). The non-linear cases also verify the time lag between the unstable, long-period gas flux and displacement oscillations, which is most pronounced for cases with

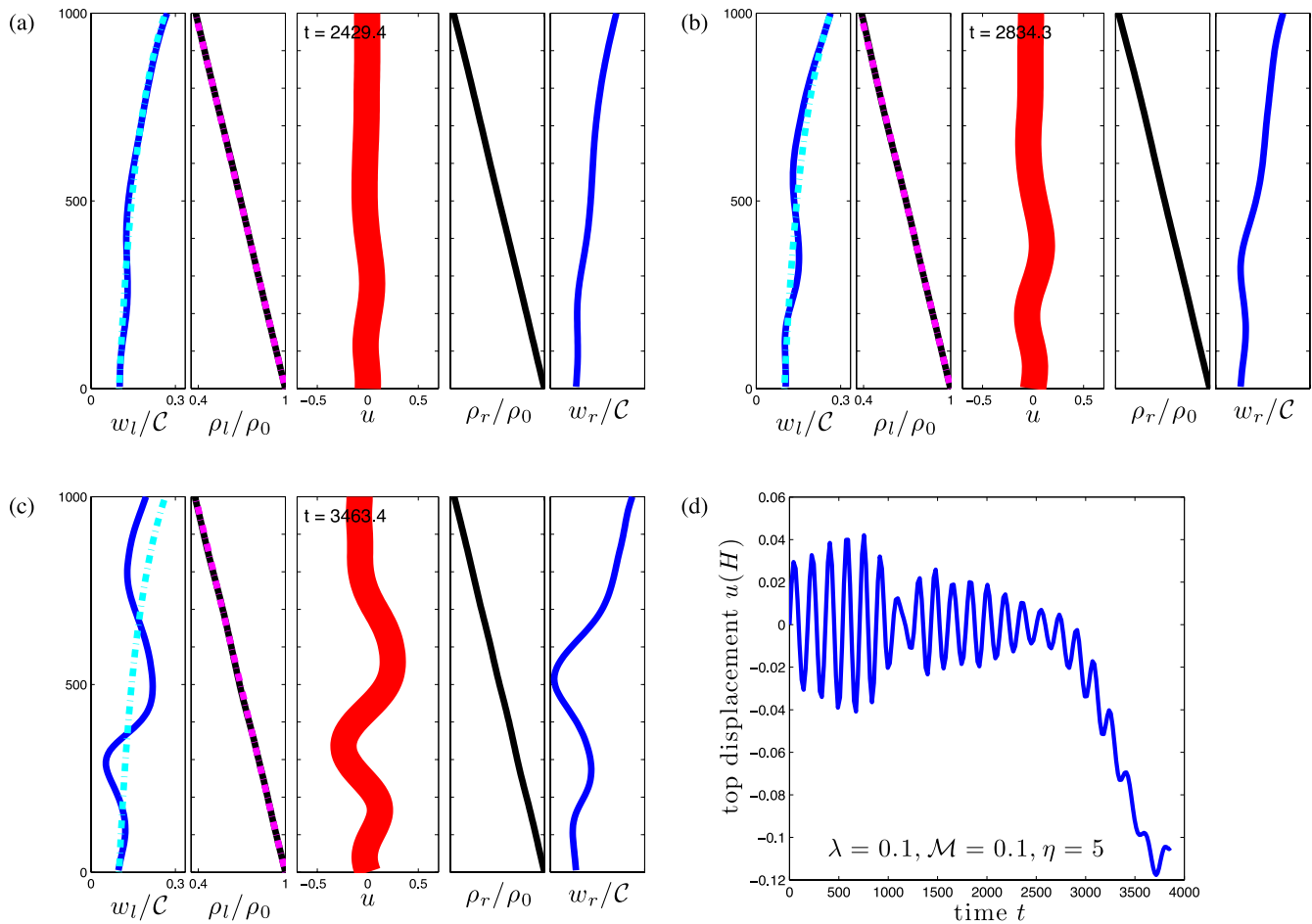


Figure 7. Snapshots of non-linear solutions (a–c) for $\lambda = 0.1$, $\mathcal{M} = 0.1$, $\eta = 5$ (which are also indicated in frame (d)). The far left and right panels in each frame show dimensionless gas velocity for the left and right annular chambers, respectively; the next inward frames show dimensionless gas density in the corresponding chambers; and the centre frame shows displacement of the magma column. Dashed lines in the left frames are the non-linear steady-state analytic solution [see (61) in Section 4.2]. Frame (d) shows the displacement of the magma column at the top ($u(H)$) as a function of time, similar to the linear cases in Fig. 5. The scales for ρ_r and w_r are the same as for the ρ_l and w_l . For all cases $\beta = 100$ and $\gamma = 2 \times 10^{-5}$ as listed in Table 1. An avi-format movie of this case is given in the Supporting Information. Also, see Fig. 2 for dimensionalizing scales.

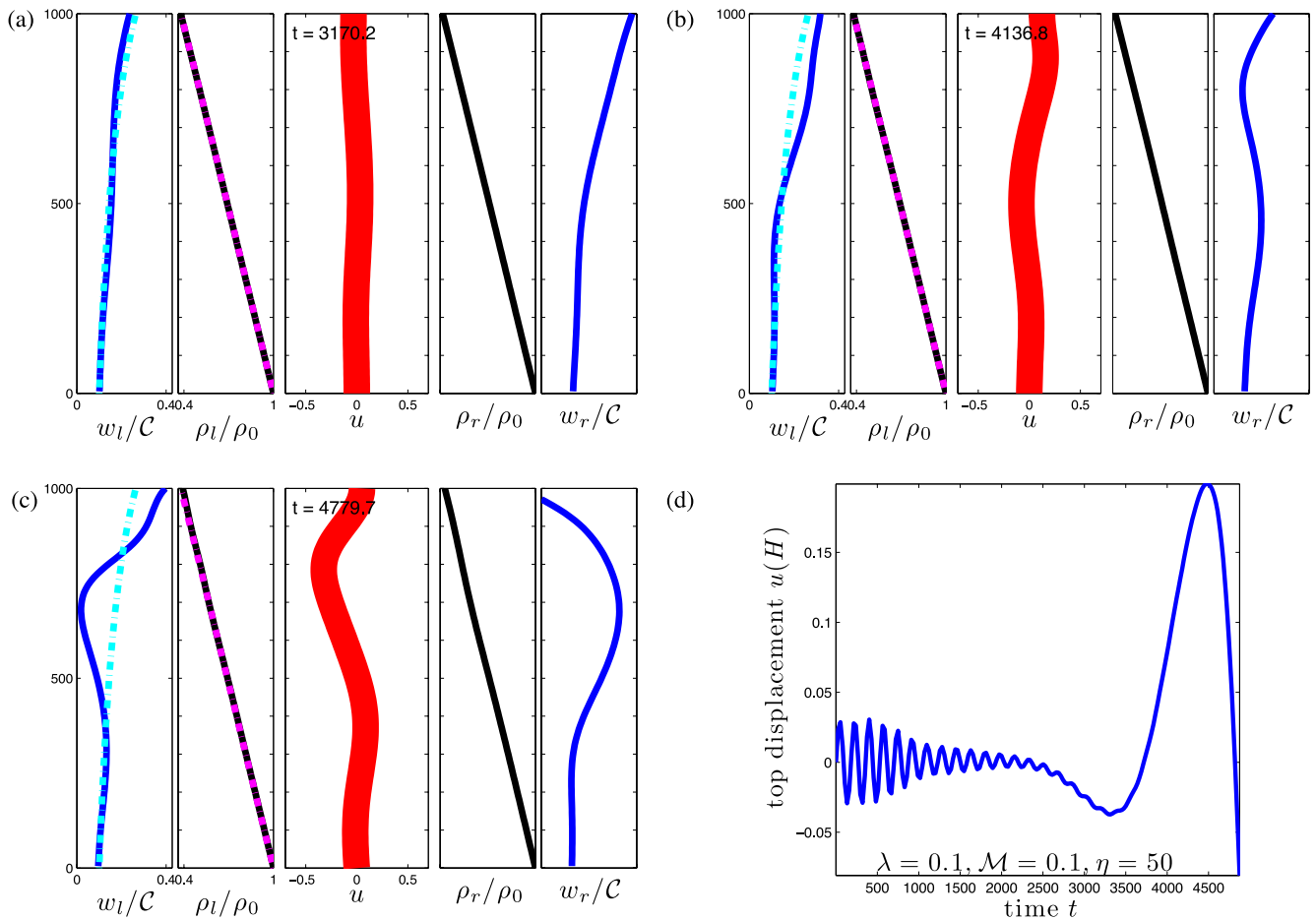


Figure 8. Same as Fig. 7 but for a higher magma column viscosity with $\eta = 50$. An avi-format movie of this case is given in the Supporting Information.

low gas injection rate \mathcal{M} , as predicted in the linear analysis (see Section 3.4.5).

The numerical cases show the initial high-frequency wagging oscillation [best seen in the time-series of $u(H)$ and the on-line movies] followed by the unstable low-frequency oscillation, which grows in amplitude until the maximum allowed displacement of $u = \phi_0$ (at which point the annulus or channel gas volume fraction drops to zero) is reached. At the maximum displacement the annulus is effectively closed at various vertical levels and the gas flux is shut off. Although the model does not track the evolution of the system beyond this point, there are two likely scenarios that follow. One possibility is that the closed annulus is reconstructed by continued ascent of the magma column, at which point the oscillation cycle starts again. Alternatively, since the non-linear model is only in one vertical plane, the oscillation might proceed in a different vertical plane that does not have a pinched annulus. This latter scenario would best be modelled by fully 3-D motion of the magma column that would allow effective nutation, wobble and helical motion in the wagging oscillation, although this is beyond the scope of this study. Nevertheless, these results suggest that after the growth of the lower-frequency oscillation, the cycle would likely begin again either with a rebuilt annulus or (perhaps more likely) in a different vertical plan (or with 3-D motion).

However, it should be noted that because of various simplifying assumptions, the non-linear model may not mitigate or saturate the nearly exponential growth of the low-frequency oscillation, as is usually expected of non-linear systems. As mentioned above,

3-D motion is suppressed, but if allowed it could possibly ease exponential growth with another degree of freedom.

5 DISCUSSION AND INTERPRETATION

The magma-wagging model with degassing-tremor interactions provides several testable predictions beyond the basic tremor frequency itself. The wagging characteristics, non-linear and unstable response and the correspondence with degassing flux lead to added features in the oscillatory behaviour that are possibly evident in seismic, acoustic and gas-emission measurements.

5.1 Spatio-temporal wagging correlation

The basic magma-wagging model proposed by Jellinek & Bercovici (2011) not only predicts the typical 1 Hz (i.e. 0.5–7 Hz) tremor oscillation, but the implicit wagging motion suggests that ground motion surrounding a volcano should be spatially and temporally correlated. That is, magma column displacement to one side will induce initial compressive ground motion in that direction, and tensile motion on the opposite side; a half an oscillation period later the sign of ground motion on either side will reverse. Thus the ground motion on opposite sides of a magma-wagging volcanic system should be well correlated after adjusting for a time lag comparable to half the wagging or tremor period. Indeed, analysis of data from seismometers on nearly opposite sides of Redoubt Volcano

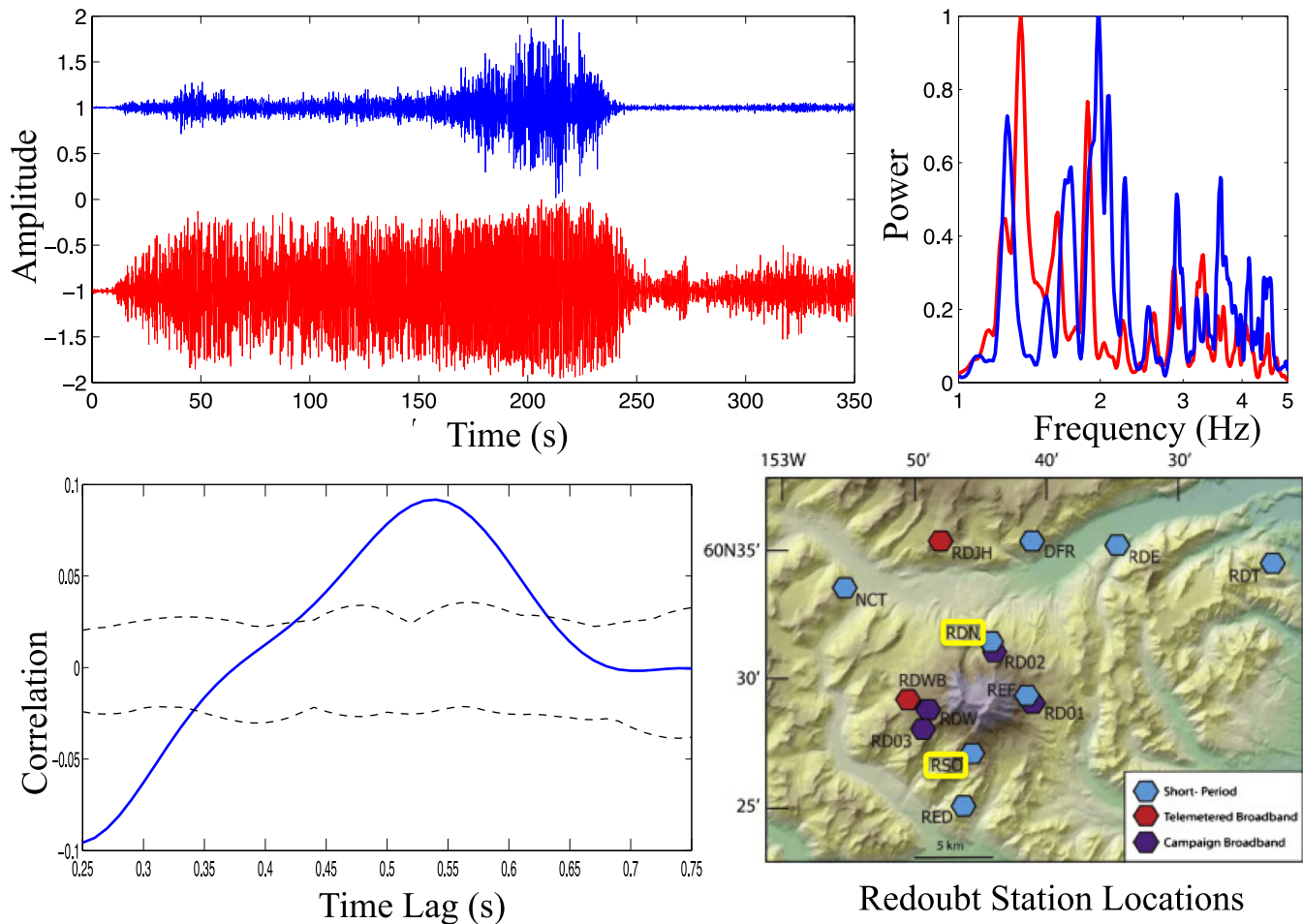


Figure 9. Comparison of tremor recorded on 2009 February 5 at Redoubt Volcano prior to the explosive eruption that began on 2009 March 22. Time-series data (top left) are from two single-vertical-component seismometers located north (blue time-series from station RDN) and south (red time-series from station RSO) of the volcano summit (station locations indicated bottom right). Raw time-series have been instrument-corrected (M. Haney, personal communication, 2013; Haney *et al.* 2012) and bandpass filtered between 1 and 5 Hz (top right). Amplitudes for the time-series and spectral data are normalized to the maximum values for the sake of comparison. The unbiased cross-correlation function (blue curve, bottom left) gives a positive correlation between the RDN and RSO signals with a time lag of about 0.55 s (with a range of 0.47–0.61 s at the half-width) with a >95 per cent confidence (dashed lines), calculated following the approach of Saar & Manga (2004) and Jellinek *et al.* (2004). This time lag is comparable to approximately half the period of the dominant signal (of order 1 s) displayed in the power-spectra (top right). Data collected by the Alaska Volcano Observatory (AVO) and retrieved from Incorporated Research Institutions for Seismology (IRIS) archives.

prior to its 2009 March eruption displays the predicted behaviour; that is, the cross-correlation of signals from the seismometers is maximized for a time lag of approximately half the dominant oscillation period (Fig. 9). This time lag might be influenced by shallow seismic velocity heterogeneity around the volcanic edifice, as well as imprecise knowledge of the location of the magma column; thus more extensive analysis is clearly warranted. Nevertheless, this case gives an intriguing example of an important first-order prediction of magma-wagging, that is, spatio-temporal correlation of tremor signals around volcanoes.

5.2 Sporadic tremor envelopes

The linear analysis of the extended magma-wagging model (including annular gas flux) predicts essentially two oscillatory modes (each has an upward and downward propagating component, thus there are really four modes for any given wavelength; see Fig. 2).

One mode is associated with the high-frequency 1 Hz oscillation that is slowly decaying, with the slowest decay occurring for the fundamental wavenumber $k_0 = \pi/(2H)$, where H is the column height. The other mode is of lower frequency (of order 0.1 Hz) but is unstable and has a maximum positive growth rate at a given k (which depends on system properties). The superposition of these two modes leads to a high-frequency oscillation riding atop a long-period, growing oscillation (Fig. 5).

The full model system, however, is fourth-order non-linear, with third- and second-order non-linearities also present; see (56)–(58) where (57) has the highest order non-linearity. Non-linear interactions between oscillations of a given frequency lead to cascading of energy to higher harmonics (e.g. Fig. 10, bottom), and given the presence of both odd and even non-linearities, all harmonics (both even and odd) are excited. The addition of harmonic and other modes leads to beating envelopes of high-frequency oscillations (e.g. see surface displacement oscillations in Figs 7 and 8, and A1–A6, frame d). An illustrative example, selected to allow

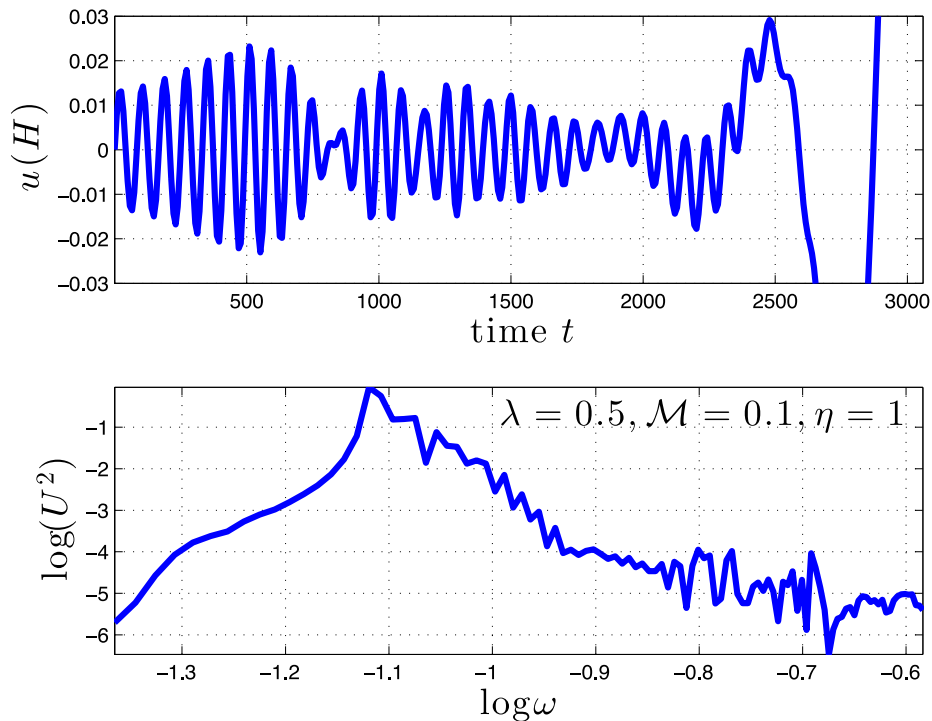


Figure 10. Time-series and power-spectrum for surface displacement for a case with $\lambda = 0.5$, $\mathcal{M} = 0.1$ and $\eta = 1$ to allow longer sampling of oscillations and their beating envelope. The power-spectrum is from a Fourier analysis of the time-series with the background growth removed; power is in terms of $U^2(\omega)$ where $U(\omega)$ is the discrete Fourier transform of $u(H)$, and ω is the discrete angular frequency.

more envelope development, shows a power-spectrum with emerging secondary frequencies only tens of per cent different from the peak frequency (Fig. 10); the superposition of these close frequencies induces the envelope structure (i.e. the envelope frequency itself is proportional to the difference in frequencies between the superposed oscillations). With the growing low-frequency mode, only a few envelopes appear before the displacement grows and reaches its maximum value (i.e. $u \leq \phi_0 L$), at which point the oscillations stop until they can potentially restart (see discussion at the end of Section 4.3.2).

This nonlinear behaviour leads to sporadic bursts of tremors, in which oscillation envelopes go unstable and cease for finite intervals of time (until, in principle, the annulus is rebuilt and the wagging oscillations start again). These sporadic envelopes are potentially seen in tremor data measured in both seismic and acoustic data (Figs 9 and 11). In particular, many time-series display sequences of growing envelopes or bursts of tremor that cease for intervals of no less than tens of seconds (see also Chouet & Matoza 2013, fig. 33); this minimum interval time is indeed comparable to the growth time for unstable low-frequency modes, which would be the minimum time between bursts predicted by the model.

5.3 Gas flux and tremor correlation

The magma-wagging model with gas-flux forcing predicts various correlations between tremor and pulses in gas flux. Observations show that short-period pulses in gas flux are nearly synchronous with tremors as audible ‘chugging’ (Benoit & McNutt 1997; Johnson & Lees 2000). Longer-period signals of average tremor amplitude and gas flux (Fig. 12) appear to show a significant lag between gas pulses and tremor, wherein large pulses in flux follow tremor activity by nearly a minute (Nadeau *et al.* 2011).

The non-linear magma-wagging results afford the best examples of both short- and long-period responses, as seen at the surface (Fig. 13). First, during peak higher-frequency wagging activity (analogous to tremor), the oscillations in column displacement are synchronous with density oscillations, since they provide the restoring force for the column wagging; for example, column displacement and squeezing of the annulus causes gas compression and increased pressure, which drives the column back in the opposite direction. Thus tremor associated with acceleration of the column will be synchronous with pulses of gas density arriving at the surface (see Fig. 13, comparing surface gas density to column displacement).

Long-period signals, however, would show a different behaviour. The biggest pulse in gas flux would be associated with the large increase in gas velocity at the end of the long-period growing oscillation. This pulse arrives after the largest tremor amplitudes (i.e. higher-frequency wagging oscillations) have occurred and begun to taper off (see Fig. 13, comparing surface gas velocity to either density or column displacement). The time lag between the gas pulse and the peak tremor activity is of order of the instability growth rate, dimensionally of order tens of seconds up to a minute. This lag is comparable to the lag observed in long-period field measurements (Fig. 12).

5.4 Gas flux forcing without magma extrusion

Finally, although the proposed driving mechanism for the wagging system is associated with gas flux and a Bernoulli effect in the permeable annulus, it does not necessarily mean that active eruptions and magma motion are needed to drive the oscillations. Provided there is some permeable pathway associated with the annulus,

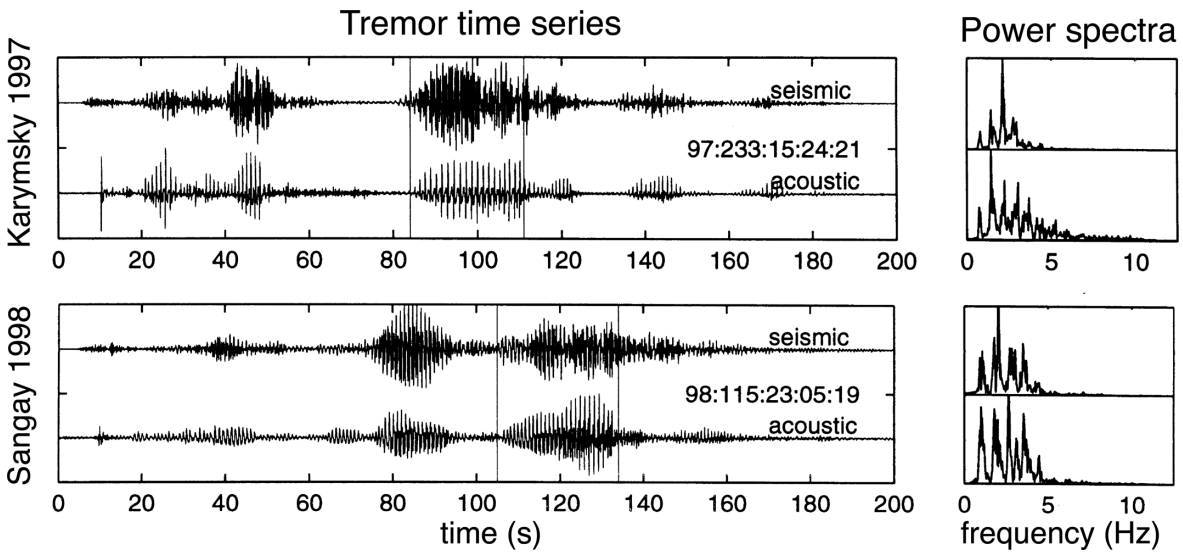


Figure 11. Time-series and power-spectrum for two volcanic events (Karymsky in 1997 and Sangay in 1998) showing sequences of growing, beating envelopes (after Johnson & Lees 2000).

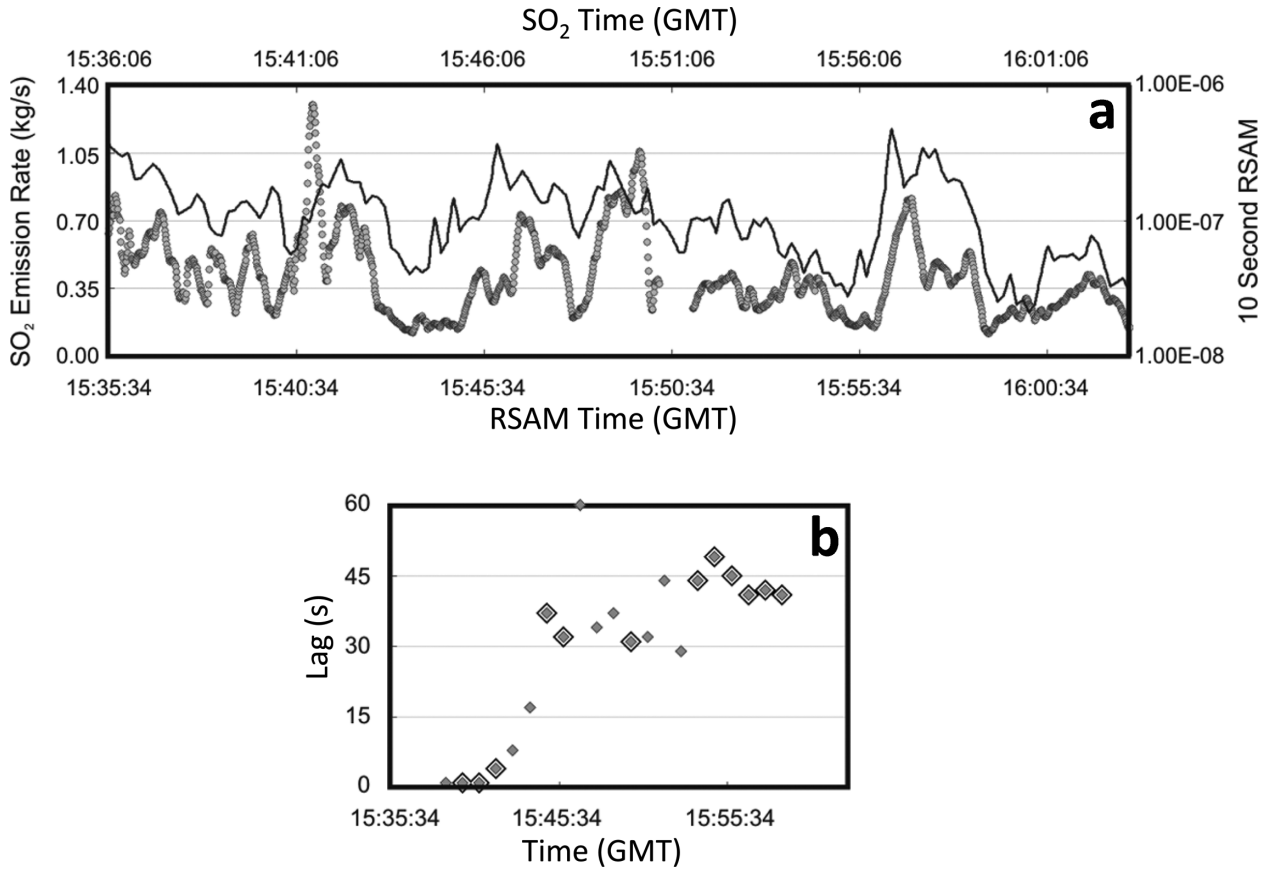


Figure 12. Time-series for both 10-s averaged tremor amplitude, and SO_2 vent gas emission rate (in kg s^{-1}) for Fuego volcano in 2009 (a); the top and bottom abscissa are offset by 32 s to compensate for overall lag. Evolution of the time lag between tremor and gas flux (b), where larger diamonds indicate correlation between time-series larger than 0.65 (after Nadeau *et al.* 2011).

gas flux from a deeper source could continue to drive the oscillation with or without magma ascent. Indeed, the typically lower gas velocities during stagnant-magma degassing would allow for longer periods of free tremor oscillations before the instability occurs. If the cessation in magma ascent causes the annulus to collapse and

the foamy magma to compact, then gas being squeezed out of the annulus could also drive the oscillation, although this would be a transient effect (and possibly fairly brief, since the timescale for collapse is of order $v_m/(gH_0)$ where H_0 is the initial column height of order 1 km).

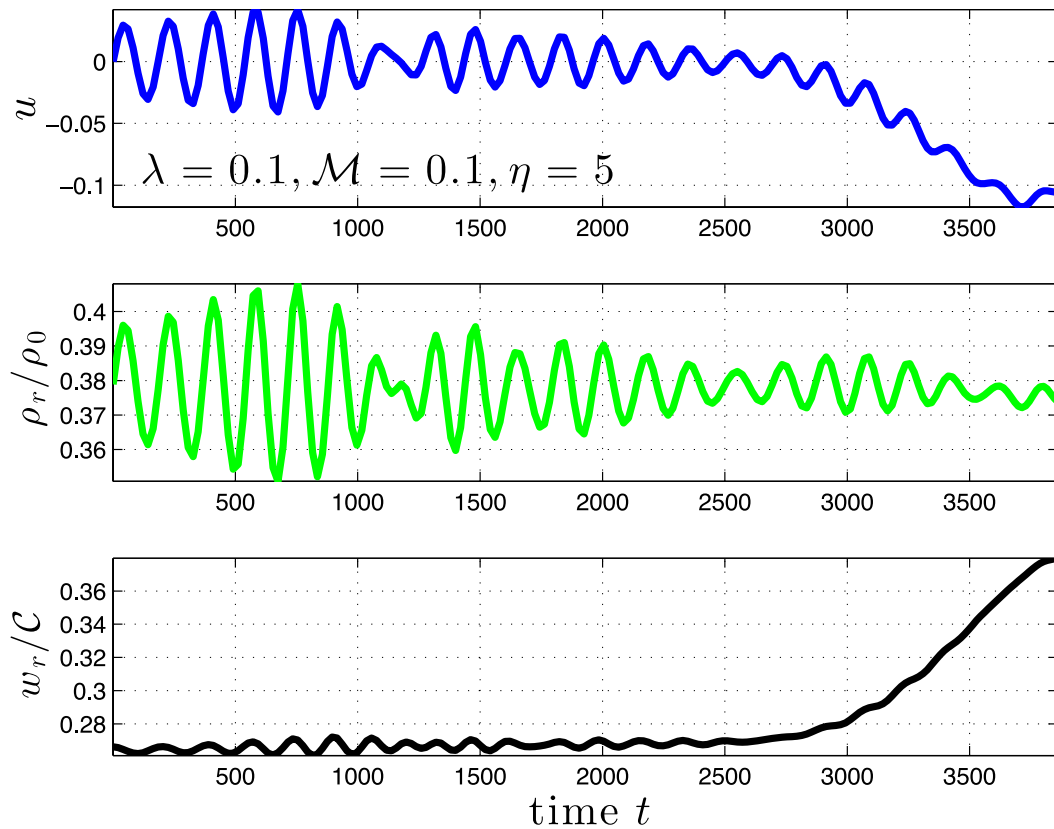


Figure 13. Time-series for surface displacement u , as well as gas density and velocity for the right annular channel $\rho_r = \rho_2$ and $w_r = w_2$, respectively, at the conduit top $z = H$. The case shown is the same as that in Fig. 7, with $\lambda = 0.1$, $\mathcal{M} = 0.1$ and $\eta = 5$. These time-series display the lag between peak tremor activity (at around dimensionless time $t = 700$) and the maximum gas flux at the end ($t \approx 4000$). Dimensionally this lag is several to several tens of seconds, depending on the annular gap width, similar to the time lag observations in Fig. 12.

6 SUMMARY AND CONCLUSION

We have presented an extended magma-wagging model for tremor and related oscillations in silicic volcanoes, primarily to address the tremor forcing mechanism and the relation between tremor and gas venting. The magma-wagging oscillation is due to the free motion of a magma column inside an annulus of foamy magma; since the annulus develops by shearing against the conduit wall, its bubbles are stretched and interconnected, and it thus contains a permeable magma matrix through which gas preferentially flows. The extended wagging model thus allows for the interaction between annular gas flow and the lateral motion of the magma column. In particular, the model demonstrates that gas flow through the annulus induces a Bernoulli effect wherein column displacement that pinches the annulus will cause higher gas velocity and hence lower pressures, which thus amplify the displacement to further pinch the annulus. This feedback drives an oscillatory instability, and thus a natural forcing mechanism for wagging motion.

The free wagging oscillation without forcing has a moderately high frequency, dimensionally between 1 and 10 Hz, characteristic of tremor, but slowly damps due to viscous bending of the magma column. The wagging oscillation is also predicted to induce ground motion on opposite sides of a volcano that are out of phase by approximately half a wagging or tremor period. Moreover, non-linear interactions cause higher frequencies to develop from the fundamental wagging frequency, and these combine to produce beating envelopes of tremors.

The forced and unstable oscillation frequency is dimensionally 0.1–1 Hz, with a growth timescale of tens of seconds to a minute.

The instability is thus likely to grow over several seconds to minutes to a peak displacement, at which point the annulus is effectively collapsed in the plane of wagging motion. With continued magma ascent and/or gas venting, the wagging motion and instability would re-start either in another plane, or with 3-D motion or after the annulus is re-established. The net effect of both oscillatory modes leads to sporadic bursts of tremor envelopes that go unstable, cease and restart with a timescale dictated by the instability growth rate (tens of seconds).

The high-frequency tremor oscillations themselves are also associated with gas density and pressure perturbations at the surface, which thus lead to degassing pulses synchronous with ground motion. Moreover, the long-period instability is punctuated by a large degassing flux that lags, by a several tens of seconds, after the peak tremor amplitudes.

In total, these model predictions correlate well with observations of time lags between seismic signals on opposite sides of a volcano, sporadic envelopes of tremor, audible degassing or ‘chugging’ coincident with tremor (Johnson & Lees 2000) and large time lags (i.e. nearly minute long) between peak tremor activity and the largest pulses in gas flux (Nadeau *et al.* 2011).

Nevertheless, a more sophisticated numerical model of the magma-wagging system is warranted for future studies. The model as it stands now only allows for 2-D motion in a plane, and thus does not account explicitly for re-starting the wagging motion after it goes unstable once. A model that allows fully 3-D motion of the gas and magma column, including, for example, azimuthal gas flow, helical motion of the column and compaction of the whole mixture

(e.g. see Michaut *et al.* 2013) would possibly allow more developed evolution of the oscillatory behaviour. However, the driving mechanism for the magma-wagging oscillation and the interaction between wagging and gas flux, are shown to arise naturally from the model, whose results remain consistent with the short-period oscillatory behaviour in silicic volcanic systems.

ACKNOWLEDGEMENTS

The authors are grateful to Stephane Labrosse and two anonymous reviewers for helpful comments and suggestions. DB was supported by the National Science Foundation (NSF, grant EAR-1015229); AMJ was supported by NSERC and the Canadian Institute for Advanced Research. We thank Matt Haney for help with the instrument response corrections, which were required to analyse the seismic data in Fig. 9.

REFERENCES

- Bagdassarov, N., Dingwell, D. & Webb, S., 1994. Viscoelasticity of crystal- and bubble-bearing rhyolite melts, *Phys. Earth planet. Inter.*, **83**(2), 83–99.
- Benoit, J. & McNutt, S., 1997. New constraints on source processes of volcanic tremor at Arenal Volcano, Costa Rica, using broadband seismic data, *Geophys. Res. Lett.*, **24**(4), 449–452.
- Bercovici, D. & Michaut, C., 2010. Two-phase dynamics of volcanic eruptions: compaction, compression, and the conditions for choking, *Geophys. J. Int.*, **182**, 843–864.
- Bluth, G. & Rose, W., 2004. Observations of eruptive activity at Santiaguito volcano, Guatemala, *J. Volc. Geotherm. Res.*, **136**(3–4), 297–302.
- Bryan, C. & Sherburn, S., 2003. Eruption-induced modifications to volcanic seismicity at Ruapehu, New Zealand, and its implications for eruption forecasting, *Bull. Volcanol.*, **65**(1), 30–42.
- Chouet, B., 1996. Long-period volcano seismicity: its source and use in eruption forecasting, *Nature*, **380**, 309–316.
- Chouet, B.A. & Matoza, R.S., 2013. A multi-decadal view of seismic methods for detecting precursors of magma movement and eruption, *J. Volc. Geotherm. Res.*, **252**(0), 108–175.
- Chouet, B., Saccorotti, G., Martini, M., Dawson, P., De Luca, G., Milana, G. & Scarpa, R., 1997. Source and path effects in the wave fields of tremor and explosions at Stromboli Volcano, Italy, *J. geophys. Res.*, **102**(B7), 15 129–15 150.
- Collier, L., Neuberg, J., Lensky, N., Lyakhovskiy, V. & Navon, O., 2006. Attenuation in gas-charged magma, *J. Volc. Geotherm. Res.*, **153**(1–2), 21–36.
- Denlinger, R. & Hoblitt, R., 1999. Cyclic eruptive behavior of silicic volcanoes, *Geology*, **27**(5), 459–462.
- Eichelberger, J.C., Carrigan, C.R., Westrich, H.R. & Price, R.H., 1986. Non-explosive silicic volcanism, *Nature*, **323**, 598–602.
- Garcés, M., Hagerty, M. & Schwartz, S., 1998. Magma acoustics and time-varying melt properties at Arenal Volcano, Costa Rica, *Geophys. Res. Lett.*, **25**(13), 2293–2296.
- Gonnermann, H.M. & Manga, M., 2007. The fluid mechanics inside a volcano, *Annu. Rev. Fluid Mech.*, **39**, 321–356.
- Goto, A., 1999. A new model for volcanic earthquake at Unzen Volcano: melt rupture model, *Geophys. Res. Lett.*, **26**(16), 2541–2544.
- Hagerty, M., Schwartz, S., Garces, M. & Pratti, M., 2000. Analysis of seismic and acoustic observations at Arenal Volcano, Costa Rica, 1995–1997, *J. Volc. Geotherm. Res.*, **101**(1–2), 27–65.
- Haney, M.M., Power, J., West, M. & Michaels, P., 2012. Causal instrument corrections for short-period and broadband seismometers, *Seism. Res. Lett.*, **83**(5), 834–845.
- Hellweg, M., 2000. Physical models for the source of Lascar's harmonic tremor, *J. Volc. Geotherm. Res.*, **101**(1–2), 183–198.
- Hotovec, A.J., Prejean, S.G., Vidale, J.E. & Gomberg, J., 2013. Strongly gliding harmonic tremor during the 2009 eruption of Redoubt Volcano, *J. Volc. Geotherm. Res.*, **259**, 89–99.
- Hurst, A. & Sherburn, S., 1993. Volcanic tremor at Ruapehu: characteristics and implications for the tremor source, *NZ J. Geol. Geophys.*, **36**, 475–485.
- Jellinek, A.M. & Bercovici, D., 2011. Seismic tremors and magma wagging during explosive volcanism, *Nature*, **470**(7335), 522–525.
- Jellinek, A.M., Manga, M. & Saar, M.O., 2004. Did melting glaciers cause volcanic eruptions in eastern California? Probing the mechanics of dike formation, *J. geophys. Res.*, **109**(B9), B09206, doi:10.1029/2004JB002978.
- Johnson, J. & Lees, J., 2000. Plugs and chugs: seismic and acoustic observations of degassing explosions at Karymsky, Russia and Sangay, Ecuador, *J. Volc. Geotherm. Res.*, **101**(1), 67–82.
- Julian, B., 1994. Volcanic tremor: nonlinear excitation by fluid flow, *J. geophys. Res.*, **99**(B6), 11 859–11 877.
- Klug, C. & Cashman, K., 1996. Permeability development in vesiculating magmas: implications for fragmentation, *Bull. Volcanol.*, **58**(2), 87–100.
- Konstantinou, K. & Schlindwein, V., 2003. Nature, wavefield properties and source mechanism of volcanic tremor: a review, *J. Volc. Geotherm. Res.*, **119**(1–4), 161–187.
- Kozono, T. & Koyaguchi, T., 2009a. Effects of relative motion between gas and liquid on 1-dimensional steady flow in silicic volcanic conduits: 1. An analytical method, *J. Volc. Geotherm. Res.*, **180**, 21–36.
- Kozono, T. & Koyaguchi, T., 2009b. Effects of relative motion between gas and liquid on 1-dimensional steady flow in silicic volcanic conduits: 2. Origin of diversity of eruption styles, *J. Volc. Geotherm. Res.*, **180**, 37–49.
- Kumagai, H. & Chouet, B., 1999. The complex frequencies of long-period seismic events as probes of fluid composition beneath volcanoes, *Geophys. J. Int.*, **138**(2), F7–F12.
- Lees, J.M., Johnson, J.B., Ruiz, M., Troncoso, L. & Welsh, M., 2008. Reventador Volcano 2005: eruptive activity inferred from seismo-acoustic observation, *J. Volc. Geotherm. Res.*, **176**(1), 179–190.
- McNutt, S., 2005. Volcanic seismology, *Annu. Rev. Earth planet. Sci.*, **32**, 461–491.
- McNutt, S. & Nishimura, T., 2008. Volcanic tremor during eruptions: temporal characteristics, scaling and constraints on conduit size and processes, *J. Volc. Geotherm. Res.*, **178**(1), 10–18.
- Michaut, C., Ricard, Y., Bercovici, D. & Sparks, R.S.J., 2013. Eruption cyclicity at silicic volcanoes potentially caused by magmatic gas waves, *Nature Geosci.*, doi:10.1038/ngeo1928.
- Nadeau, P.A., Palma, J.L. & Waite, G.P., 2011. Linking volcanic tremor, degassing, and eruption dynamics via SO₂ imaging, *Geophys. Res. Lett.*, **38**, L01304, doi:10.1029/2010GL045820.
- Neuberg, J., 2000. Characteristics and causes of shallow seismicity in andesite volcanoes, *Phil. Trans. R. Soc. Lond. Series A: Math Phys. Eng. Sci.*, **358**(1770), 1533–1546.
- Neuberg, J., Tuffen, H., Collier, L., Green, D., Powell, T. & Dingwell, D., 2006. The trigger mechanism of low-frequency earthquakes on Montserrat, *J. Volc. Geotherm. Res.*, **153**(1–2), 37–50.
- Okumura, S., Nakamura, M. & Tsuchiyama, A., 2006. Shear-induced bubble coalescence in rhyolitic melts with low vesicularity, *Geophys. Res. Lett.*, **33**(20), L20316, doi:10.1029/2006GL027347.
- Okumura, S., Nakamura, M., Tsuchiyama, A., Nakano, T. & Uesugi, K., 2008. Evolution of bubble microstructure in sheared rhyolite: formation of a channel-like bubble network, *J. geophys. Res.: Solid Earth*, **113**(B7), B07208, doi:10.1029/2007JB005362.
- Roache, P.J., 1976. *Computational Fluid Dynamics*, Hermosa, Albuquerque, NM.
- Rust, A., Balmforth, N. & Mandre, S., 2008. The feasibility of generating low-frequency volcano seismicity by flow through a deformable channel, *Geol. Soc. Lond. Spec. Publ.*, **307**(1), 45–56.
- Saar, M. & Manga, M., 2004. Depth dependence of permeability in the Oregon Cascades inferred from hydrogeologic, thermal, seismic, and magmatic modeling constraints, *J. geophys. Res.*, **109**(B4), B04204, doi:10.1029/2003JB002855.

- Sahetapy-Engel, S.T. & Harris, A.J., 2009. Thermal structure and heat loss at the summit crater of an active lava dome, *Bull. Volcanol.*, **71**(1), 15–28.
- Sherburn, S., Bryan, C., Hurst, A., Latter, J. & Scott, B., 1999. Seismicity of Ruapehu volcano, New Zealand, 1971–1996: a review, *J. Volc. Geotherm. Res.*, **88**(4), 255–278.
- Sparks, R., 2003. Dynamics of magma degassing, *Geol. Soc. Lond. Spec. Publ.*, **213**(1), 5–22.
- Stasiuk, M.V., Barclay, J., Carroll, M.R., Jaupart, C., Ratté, J.C., Sparks, R.S.J. & Tait, S.R., 1996. Degassing during magma ascent in the Mule Creek Vent (USA), *Bull. Volcanol.*, **58**, 117–130.
- Tuffen, H., Smith, R. & Sammonds, P., 2008. Evidence for seismogenic fracture of silicic magma, *Nature*, **453**(7194), 511–514.
- Vergnolle, S. & Jaupart, C., 1986. Separated two-phase flow and basaltic eruptions, *J. geophys. Res.*, **91**, 12 842–12 860.
- Wright, H., Roberts, J. & Cashman, K., 2006. Permeability of anisotropic tube pumice: model calculations and measurements, *Geophys. Res. Lett.*, **33**(17), L17316, doi:10.1029/2006GL027224.
- Wright, H., Cashman, K., Gottesfeld, E. & Roberts, J., 2009. Pore structure of

- volcanic clasts: measurements of permeability and electrical conductivity, *Earth planet. Sci. Lett.*, **280**(1–4), 93–104.
- Zobin, V.M., 2011. *Introduction to Volcanic Seismology*, Elsevier.

APPENDIX: ADDITIONAL NON-LINEAR 2-D RESULTS

The non-linear results of the 2-D magma-wagging model with annular channel gas flux are discussed in Section 4.3.2. Figs 7 and 8 display results for a moderate gap-width aspect-ratio $\lambda = L/(2R_m) = 0.1$, low gas injection Mach number $\mathcal{M} = W_0/C = 0.1$ and two different dimensionless magma viscosities $\eta = \nu_m/(CL) = 5$ and 50. Here, for completeness, we display two more cases for the same values of λ and η , but a larger injection flux $\mathcal{M} = 0.5$ (Figs A1 and A2). In addition, we show four more cases for a narrower gap aspect $\lambda = 0.01$, and the same combinations of $\eta = 5$ or 50 and $\mathcal{M} = 0.1$ or 0.5 (Figs A3–A6).

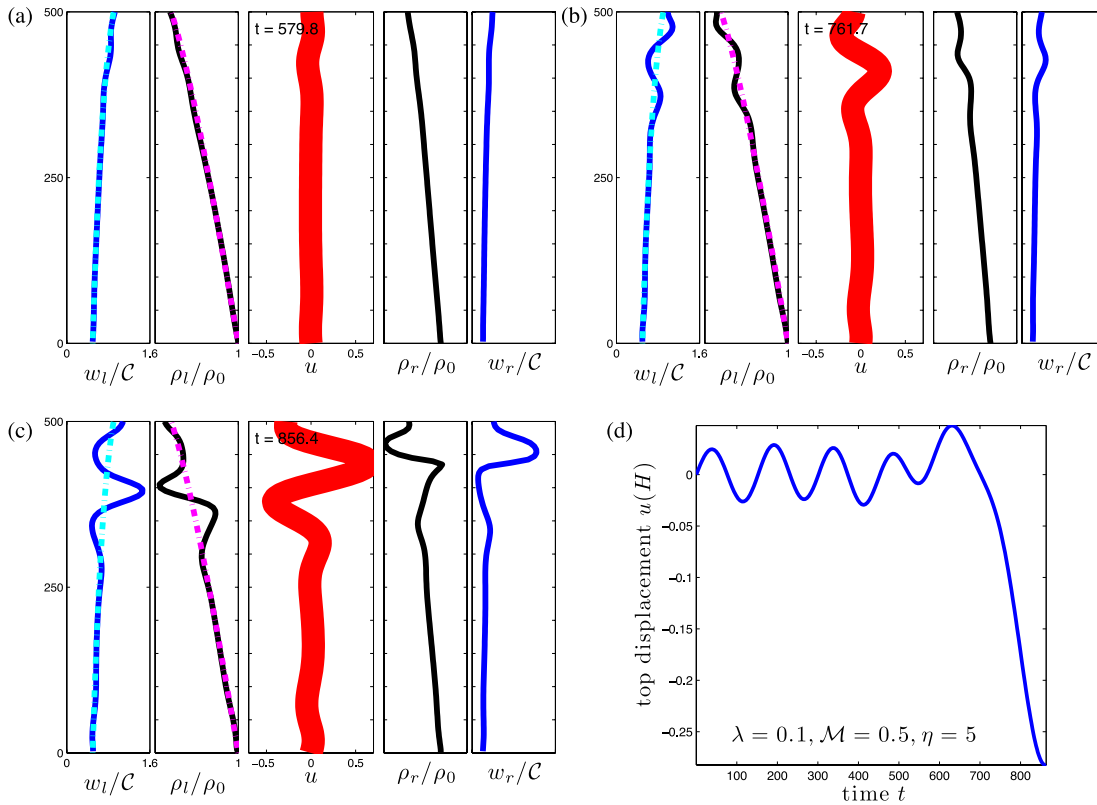


Figure A1. Same as Fig. 7 but for a higher gas injection velocity $\mathcal{M} = 0.5$. An avi-format movie of this case is given in the Supporting Information.

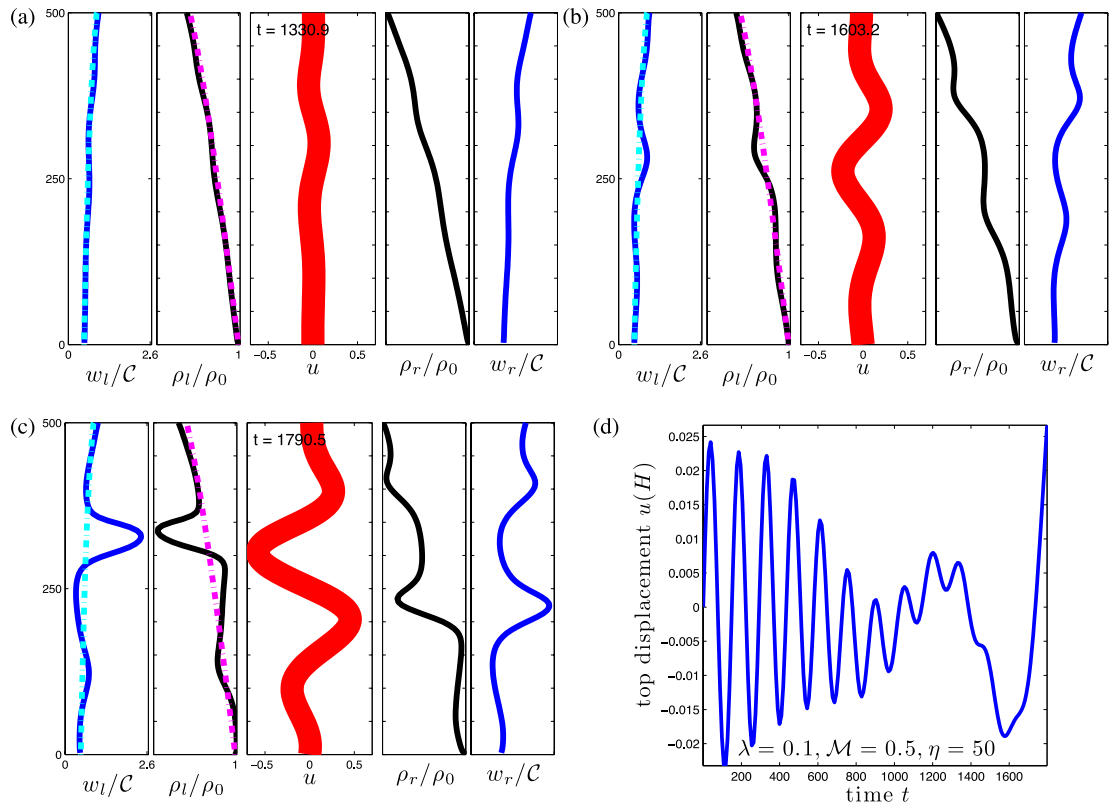


Figure A2. Same as Fig. 7 but for both a higher gas injection velocity $\mathcal{M} = 0.5$ and magma column viscosity $\eta = 50$. An avi-format movie of this case is given in the Supporting Information.

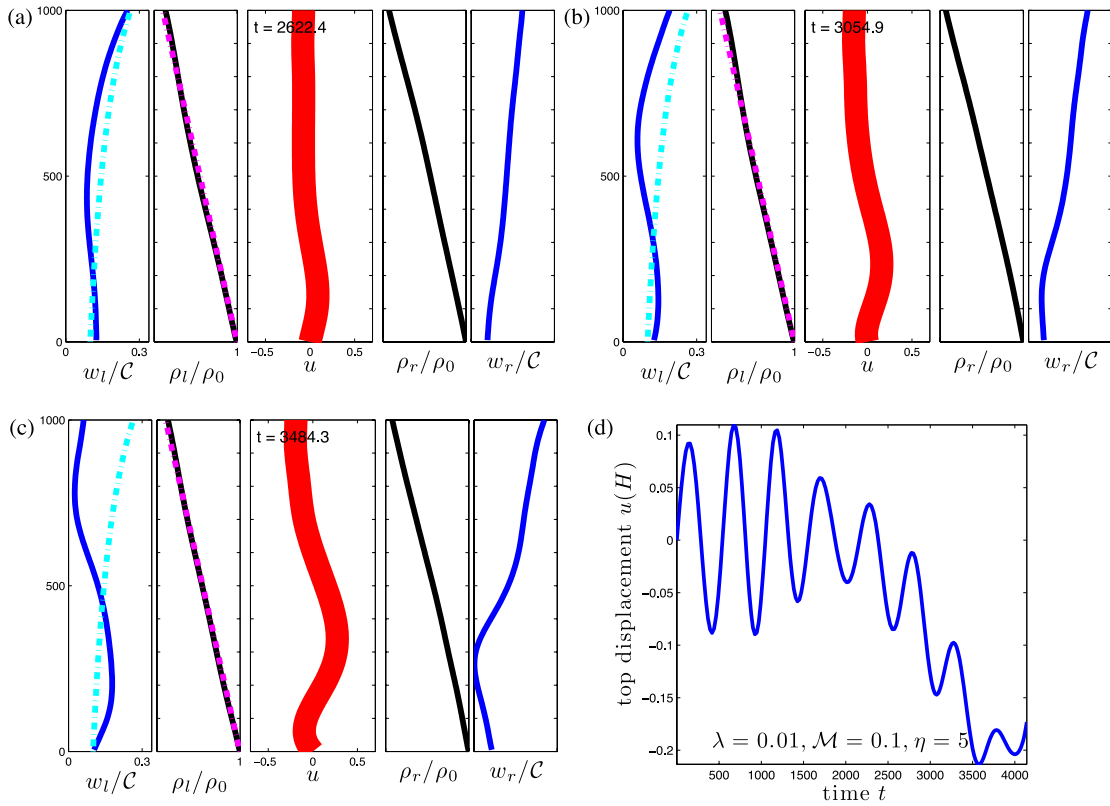


Figure A3. Same as Fig. 7 but for a narrow gap aspect ratio $\lambda = 0.01$. An avi-format movie of this case is given in the Supporting Information.

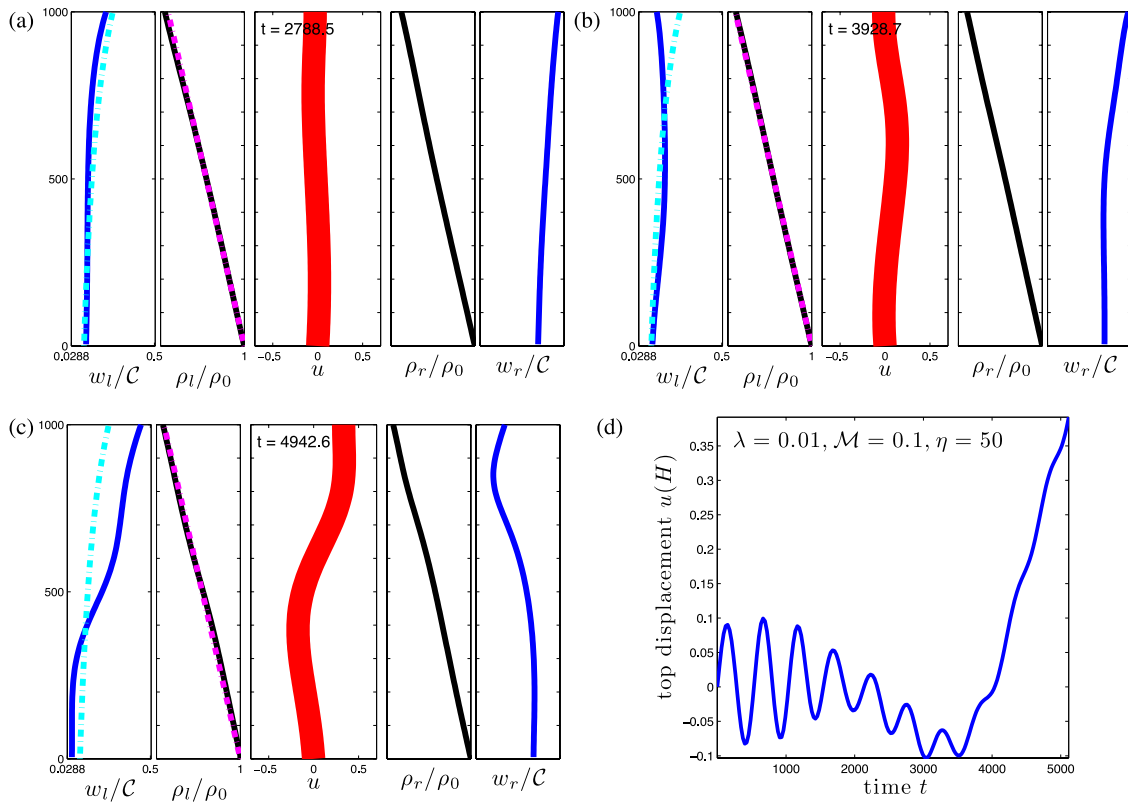


Figure A4. Same as Fig. 7 but for a narrow gap aspect ratio $\lambda = 0.01$ and larger magma column viscosity $\eta = 50$. An avi-format movie of this case is given in the Supporting Information.

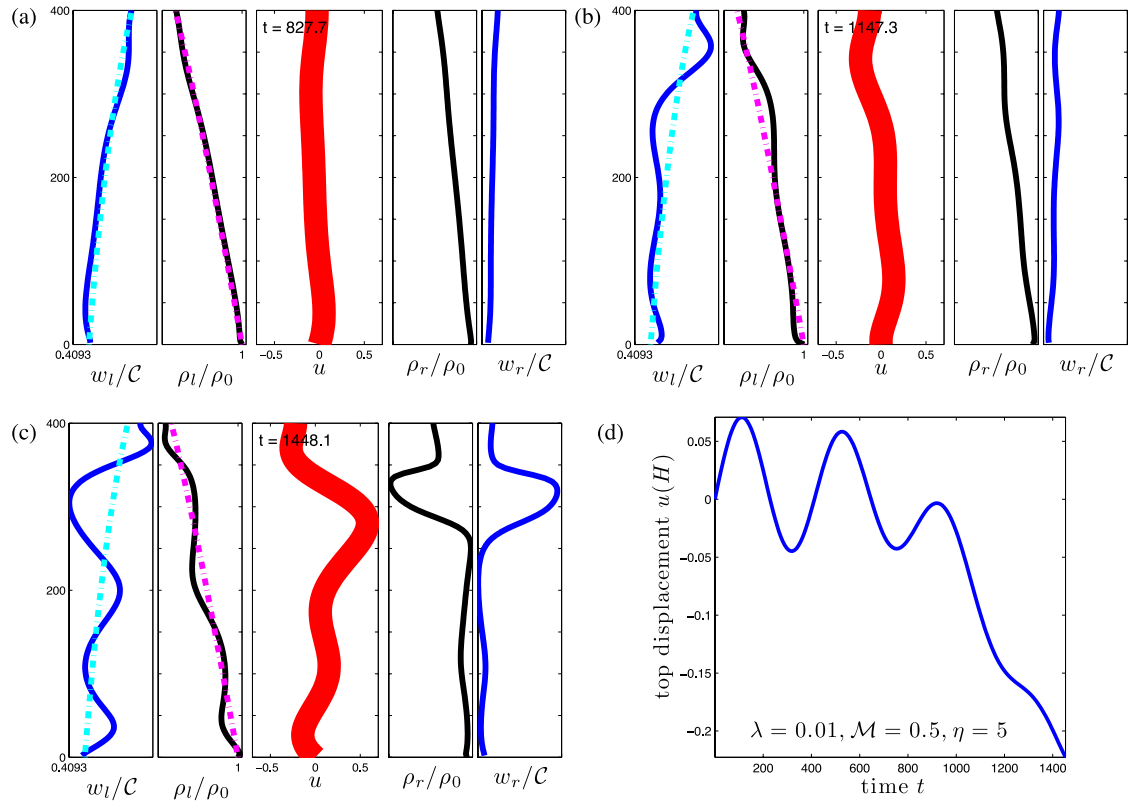


Figure A5. Same as Fig. 7 but for a narrow gap aspect ratio $\lambda = 0.01$ and larger gas injection velocity with $\mathcal{M} = 0.5$. An avi-format movie of this case is given in the Supporting Information.

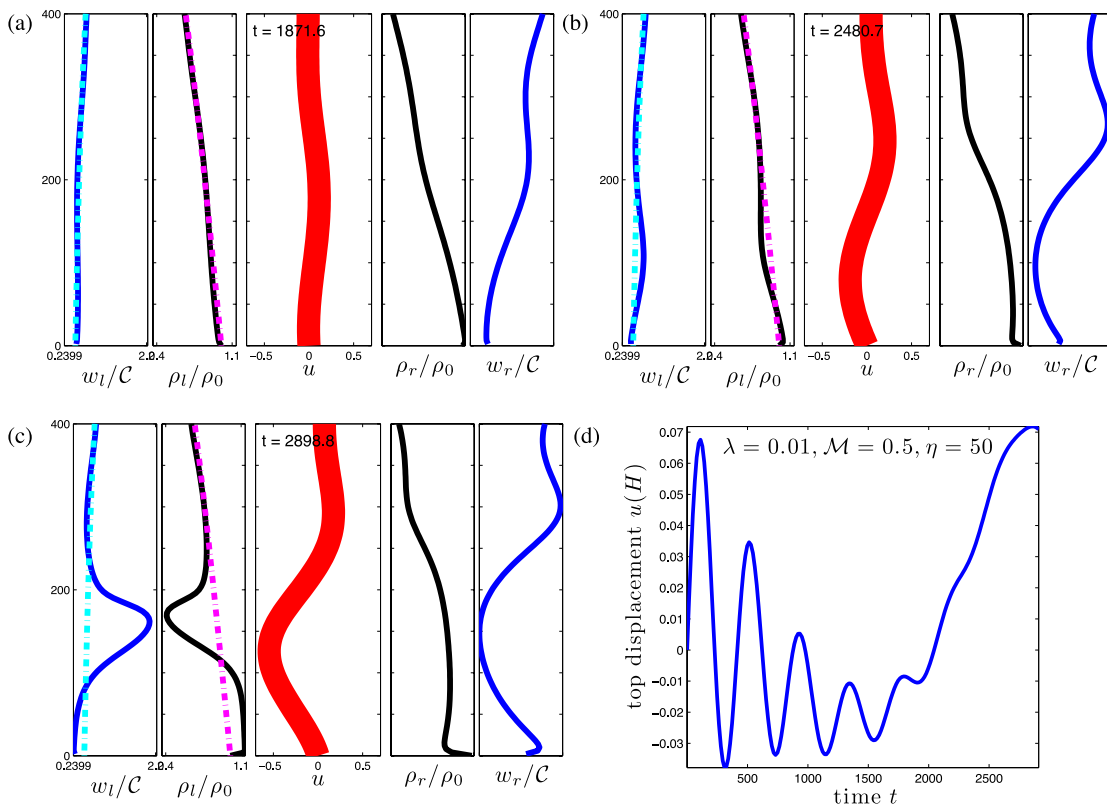


Figure A6. Same as Fig. 7 but for a narrow gap aspect ratio $\lambda = 0.01$ and both larger magma column viscosity with $\eta = 50$ and gas injection velocity with $\mathcal{M} = 0.5$. An avi-format movie of this case is given in the Supporting Information.

SUPPORTING INFORMATION

Additional Supporting Information may be found in the online version of this article:

Movies S1–S8. Animations of the numerical solutions displayed in Figures 7, 8 and A1–A6 (<http://gji.oxfordjournals.org/lookup/suppl/doi:10.1093/gji/ggt277/-/DC1>).

Please note: Oxford University Press is not responsible for the content or functionality of any supporting materials supplied by the authors. Any queries (other than missing material) should be directed to the corresponding author for the article.